Development of a fully integrated falling film microreactor for gas-liquid-solid biotransformation with surface immobilized O_2-dependent enzyme

Juan M. Bolivar[1], Christina E. M. Krämer[1], Birgit Ungerböck[2], Torsten Mayr[2], and Bernd Nidetzky[1,3*]

[1] Institute of Biotechnology and Biochemical Engineering, Graz University of Technology, NAWI Graz, Petersgasse 12, A-8010 Graz, Austria

[2] Institute of Analytical and Food Chemistry, Graz University of Technology, Stremayrgasse 16, A-8010 Graz, Austria

[3] Austrian Centre of Industrial Biotechnology, Petersgasse 14, A-8010 Graz, Austria

* Corresponding author

Phone: +43 316 873 8400; fax: +43 316 873 8434; e-mail: bernd.nidetzky@tugraz.at

Running title: Biocatalytic falling film microreactor

Abbreviations used:

DAAO, D-amino acid oxidase; *Tv*DAAO, DAAO from the yeast *Trigonopsis variabilis*;

Z_{basic2}_*Tv*DAAO, fusion protein between the surface binding module Z_{basic2} and *Tv*DAO;

FFMR, falling film microreactor

Abstract

Microstructured flow reactors are powerful tools for the development of multiphase biocatalytic transformations. To expand their current application also to O_2 dependent enzymatic conversions, we have implemented a fully integrated falling film microreactor that provides controllable countercurrent gas-liquid phase contacting in a multi-channel microstructured reaction plate. Advanced non-invasive optical sensing is applied to measure liquid-phase oxygen concentrations in both in- and out-flow as well as directly in the microchannels (width: 600 µm; depth: 200 µm). Protein-surface interactions are designed for direct immobilization of catalyst on microchannel walls. Target enzyme (here: D-amino acid oxidase) is fused to the positively charged mini-protein Z_{basic2} and the channel surface contains a negatively charged γ-Al_2O_3 wash-coat layer. Non-covalent wall attachment of the chimeric Z_{basic2}_oxidase resulted in fully reversible enzyme immobilization with fairly uniform surface coverage and near complete retention of biological activity. The falling film at different gas and liquid flow rates as well as reactor inclination angles was shown to be mostly wavy laminar. The calculated film thickness was in the range $0.5 - 1.3 \times 10^{-4}$ m. Direct O_2 concentration measurements at the channel surface demonstrated that the liquid side mass transfer coefficient (K_{L}) for O_2 governed the overall gas/liquid/solid mass transfer and that the O_2 transfer rate (≥ 0.75 mM·s^{-1}) vastly exceeded the maximum enzymatic reaction rate in a wide range of conditions. A value of 7.5 (± 0.5) s^{-1} was determined for the overall mass transfer coefficient $K_{\mathrm{L}}a$, comprising a K_{L} of about 7×10^{-5} m·s^{-1} and a specific surface area of up to 10^5 m^{-1}.

Keywords: Falling-film microreactor; microchannel; gas/liquid/solid biotransformation; oxygen mass transfer; immobilized oxidase; Z_{basic2} binding module.

Introduction

Oxidations are key transformations of synthetic organic chemistry. O_2 is a powerful and benign oxidant, and its use supports the development of clean and safe oxidation processes (Mallat and Baiker, 2004; Podgoršek et al., 2009; Punniyamurthy et al., 2005; Que and Tolman, 2008; Sheldon et al., 2002; Sheldon, 2015; Shi et al., 2012). However, control of reactivity and selectivity of O_2 is a problem. Enzymes are masterful in their ability to activate and precisely target the oxidation power of O_2. They have therefore attracted high interest as green oxidation catalysts (Hall and Bommarius, 2011; Hollmann et al., 2011; Monti et al., 2011; Turner, 2011). Almost any biocatalytic process development starts at small scale (Tufvesson et al., 2013; Woodley, 2006). Screening and reaction optimization are often performed in volumes smaller than 1 mL (Fernandes, 2010; Wohlgemuth et al., 2015). However, mixing and other transport phenomena are often weakly defined in small-scale reactors, and this complicates rigorous analysis of the main factors of process performance (Günther and Jensen, 2006; Tufvesson et al., 2013). Multiphase reactions, in particular those involving high resistance to mass transfer across phase boundaries, are affected strongly under variable mixing conditions (Bolivar and Nidetzky, 2013; Günther and Jensen, 2006; Hartman and Jensen, 2009; Hessel et al., 2005). Gas-to-liquid O_2 transfer is often rate limiting overall in O_2 dependent transformations (Dencic et al., 2011; Garcia-Ochoa and Gomez, 2009; Gemoets et al., 2016; Lundemo and Woodley, 2015; Tomaszewski et al., 2014a; Tomaszewski et al., 2014b).

Microstructured reactors differ from reactors of conventional geometry (e.g. vessel) by an internal network of microchannels less than 1 mm wide (Bolivar et al., 2011; Bolivar and Nidetzky, 2013; Hessel et al., 2005; Wohlgemuth et al., 2015). Fluid flow in microchannels is usually directed, highly symmetric, and mostly laminar. Multiphase flows result from bringing (partially) immiscible fluids into contact while flowing through a channel microstructure (Bolivar and Nidetzky, 2013; Günther and Jensen, 2006; Hartman and Jensen, 2009). Their ability to provide well-controlled phase contacting at microscale, therefore, makes microstructured reactors powerful engineering tools for multiphase biocatalytic process development. (Bolivar and Nidetzky, 2013; Günther and Jensen, 2006). While a number of flow microreactor studies have been performed on liquid-liquid two-phase biotransformations, clearly demonstrating high potential of the microscale systems for reaction characterization and (early stage) process development (Bolivar and Nidetzky, 2013; Hessel et al., 2014), little work has been done on O_2 dependent gas-liquid two-phase oxidations in microstructured biocatalytic reactors (Bolivar et al., 2011; Bolivar and Nidetzky, 2013; Dencic et al., 2011; Dencic et al., 2012; Gutmann et al., 2015; Illner et al., 2014; Kawakami et al., 1989a; Kawakami et al., 1989b; Tomaszewski et al., 2014a; Tomaszewski et al., 2014b).

Microreactors for gas-liquid (or gas-liquid-solid) operations are categorized according to the principles of bringing the fluid phases into contact (Bolivar and Nidetzky, 2013; Hessel et al., 2005; Kashid et al., 2011; Kashid and Kiwi-Minsker, 2009; Kashid and Kiwi-Minsker, 2009; Zhang et al., 2009). One approach is to maintain the phases continuous and apply the reactor to create interface between them (Bolivar and Nidetzky, 2013; Günther and Jensen, 2006). Another is to disperse one phase into the other (Bolivar and Nidetzky, 2013; Günther and Jensen, 2006; Kashid and Kiwi-Minsker, 2009). In continuous-phase microreactors, the gas and liquid phases form two streams that enter, and usually also exit, the reactor separately. Reactors are designed to create and stabilize a thin liquid film in conjunction with a gas-liquid interface. Major advantages of continuous phase contacting are that the phases are not intermixed and that the interface is usually well defined. Continuous phase contacting was therefore preferred to characterize gas-liquid two-phase biotransformations (Kashid et al., 2011; Sobieszuk et al., 2012). The falling-film microreactor (FFMR) presents a prominent design where the liquid film is formed by liquid feed falling under gravity down a microstructured solid surface. High gas-to-liquid transfer rates are obtained thus (Commenge et al., 2006; Commenge et al., 2011; Hessel et al., 2005; Illner et al., 2014; Jähnisch et al., 2004; Mhiri et al., 2011; Monnier et al., 2010; Monnier and Falk, 2011; Rebrov et al., 2012; Yeong et al., 2004; Zanfir et al., 2005). Besides its use for reaction characterization, the FFMR has also been applied to production using scale-out as well as scale-up strategies (Hessel et al., 2005; Pennemann et al., 2004).

Here we report first-time development of a fully integrated immobilized enzyme FFMR for biocatalytic O_2 dependent oxidations. The basic FFMR from IMM (Institut für Mikrotechnik Mainz GmbH) was used. The key part of the FFMR is a multi-channel stainless steel plate on which the falling film is generated. A similar FFMR has recently been applied to homogenous oxidation of glucose catalyzed by glucose oxidase (Illner et al., 2014). However, detailed characterization of the gas-liquid phase contacting has not been performed and the enzyme immobilization in the FFMR has not been addressed. We describe a generally applicable approach of microscale enzyme immobilization on this plate. Charge complementarity between protein and plate surface is exploited to achieve a non-covalent and stable, yet readily reversible attachment of the target enzyme on microchannel walls. Channel walls are wash-coated with a layer of γ-Al_2O_3 whose hydrated surface develops negative net charge due to aluminolate groups. Fusion to a positively charged mini-protein (Z_{basic2}) is used to graft tailored surface binding properties on the enzyme of interest (here: D-amino acid oxidase, DAAO). The Z_{basic2} function as a discrete surface binding module to attach the fusion protein on the negatively charged surface in a controlled orientation. Integration of optochemical sensors for O_2 concentration determination in the liquid phase represented another crucial step of biocatalytic FFMR development. We report characterization of the FFMR in terms of hydrodynamics and gas-liquid O_2 transfer, and show microreactor application to the study of O_2 dependent oxidative deamination of D-amino acids catalyzed by DAAO.

Materials and Methods

Basic Set-up of FFMR (Figure 1)

A commercial Falling Film Microreactor (FFMR-Standard) from IMM (Mainz, Germany) was used. The assembled reactor was equipped with a stainless steel (1.4571) housing (120 × 76 × 40 mm) containing a glass viewport for visual inspection and optical analysis. The housing held a reaction plate containing 32 linear microchannels (from wet-chemical etching) exhibiting elliptically shaped bottom and overall dimension of 7.6 cm length (L_C), 600 µm width (w_C), and 200 µm depth (d_C). If not mentioned otherwise, this standard plate was used. The channel surface in each plate was coated with a 20-µm wash-coat layer of γ-Al_2O_3. The specific channel surface of the standard plate was 70 $m^2 \cdot g^{-1}$ as declared by the supplier. Height (δ_G) and width (w_G) of the gas chamber were 5.9 mm and 26 mm. Liquid volume of the FFMR was 250 µL (standard plate), about 1/40 that of the gas chamber volume. An additional microchannel copper plate was used for heat transfer between the reaction plate and an external water circuit applied for temperature control.

Liquid feed to the FFMR was controlled from pumps at reactor inlet and outlet. Pulsation of conventional peristaltic pumps was a problem. The reactor inflow was therefore connected to a pulsation-free Knauer Smartline 1000 pump delivering a minimum liquid flow rate of 7.08×10^{-10} $m^3 \cdot s^{-1}$. Reactor outflow was connected to a low-pulsation Ismatec MC-360 peristaltic pump. Liquid flow rates (Q_L) of $0.8 - 8.5 \times 10^{-8}$ $m^3 \cdot s^{-1}$ were used. O_2 impermeable polyetheretherketone tubings were used for liquid flow. Flow-through O_2 sensing devices were fitted to in- and outflow tubes. Gas flow (Q_G) was delivered with a Bronkhorst EL-flow select mass flow meter/controller in the range $0.83 - 8.33 \times 10^{-7}$ $m^3 \cdot s^{-1}$. Inclination of the FFMR was varied between 5° and 90°. Water was circulated with a Julabo F25 water bath. Photographs showing the FFMR set-up are given in Supporting Information (Figure S1).

Enzyme Immobilization

A chimeric protein termed Z_{basic2}_*Tv*DAAO was used (Wiesbauer et al., 2011). It results from fusion of the mini-protein Z_{basic2} to the N-terminus of *Tv*DAAO. Z_{basic2}_*Tv*DAAO was produced recombinantly in *E. coli* using reported procedures. Purified *Z*$_{\text{basic2}}$_*Tv*DAAO has a specific activity of 71 units/mg protein (Wiesbauer et al., 2011). The cell free extract was prepared in 50 mM potassium phosphate buffer (pH 8.0) and contained 10 mg protein/mL and 30 units of DAAO activity/mL. It was used for enzyme immobilization without purification. Immobilization conditions were those established earlier for oriented immobilization of *Z*$_{\text{basic2}}$_*Tv*DAAO on underivatized glass (Bolivar et al., 2015; Bolivar and Nidetzky, 2012b). The immobilization principle is ionic adsorption of Z$_{\text{basic2}}$ on the negatively charged surface. It may be noted that the immobilization is highly selective for the target protein under the conditions used. Therefore, despite other proteins being present in the cell free extract, it is mainly the *Z*$_{\text{basic2}}$_*Tv*DAAO that becomes immobilized. Briefly, the enzyme solution (4.4 – 6.4 mg protein/mL in potassium phosphate buffer, pH 8.0) contained 1.0 M NaCl and was supplemented with 0.5% Tween 20 (by volume). Immobilization was done under flow, by recirculating the enzyme solution (1 - 5 mL) over the microplate at different flow rates as shown later in the Results. Note that instead of the HPLC pump used for substrate feed, a syringe pump (model 88803, Bioblock Scientific) was employed to reduce foaming. Alternatively, enzyme solution (5 mL) was pipetted directly onto the plate placed into the reactor housing with the glass window removed. Using gentle agitation with a microtiter plate shaker, enzyme was allowed to soak into the microchannels. Samples were taken at certain times in both settings, and soluble protein and DAAO activity were measured in the supernatant. Washing was done by rinsing the plate with 50 mM potassium phosphate buffer (pH 7.0) containing 0.50 M NaCl until neither DAAO activity nor protein was detectable in the out-flow. The flow rate applied during washing was in the range 0.23 – 1.56 mL/min.

The protein and activity amounts immobilized on the plate were calculated from the respective balance in solution. Under otherwise constant immobilization conditions, the amount of enzyme activity loaded on the microchannel plate was highly reproducible (S.D. ≤ 7%) using the procedures just described.

External Oxygen Concentration Measurement

A fiber optic microsensor system was used for off-line determination of O_2 concentrations. It consisted of a Presens PC-controlled Microx TX3-AOT oxymeter equipped with a needle NTH microptode sensor also from Presens. Measurements in flow were conducted with the same oxymeter using a FTCH flow-through cell housed microsensor or a FireSting O_2 oxymeter from PyroScience equipped with a WE6 flow-through cell. The Pyroscience sensor, which uses a dye coated capillary instead of an optical fiber, was found to be robust and functional in a wide range of flow rates tested up to 8.5×10^{-8} $m^3 \cdot s^{-1}$.

Local Oxygen Concentration Measurement

Modular luminescence lifetime imaging was used to determine dissolved O_2 concentrations directly on the surface of the microchannels. The measurement principle has been reported before (Moser et al., 2006), but it has not been applied for in-line sensing in microreactors. Using previously reported (Fercher et al., 2011) phosphorescent nanoparticles (≤ 100 nm) were prepared from Eudragit RL-100 (Merck) through incorporation of the O_2 sensitive platinum luminescence dye (PtT975; Frontier Science) together with the dye brightness enhancer Macrolex Fluorescent Yellow FP (Simon & Werner GmbH). In experiments described in the Supporting Information, different protocols were evaluated regarding stable attachment of nanoparticles onto the γ-Al_2O_3 layered surface of the microchannels. We found that the immobilization order, enzyme prior to nanoparticles, was important (see details in the Supporting Information). About 50 µL of nanoparticle suspension (10 mg/mL) was carefully distributed over the horizontally positioned reaction plate, which was then soaked for about 120 min at 8°C. The plate was then placed into the microreactor housing and rinsed exhaustively with buffer under flow conditions. It was checked by fluorescence microscopic analysis that the nanoparticles had been distributed suitably across the different channels and along their length. It was also confirmed that nanoparticles were not washed off under flow.

For in-line measurement of the O_2 concentration the fully assembled microreactor was used. The glass window of the FFMR was replaced by a thin PET-foil (Mylar®, Goodfellow) whose thickness of 150 µm was selected to minimize losses of emitted light. Spatially resolved phosphorescence lifetime data were acquired using rapid lifetime determination as described previously (Moser et al., 2006) with a fast gate-able CCD camera (SensiCam, PCO, Germany) equipped with a RG645 optical filter from Schott (http://www.schott.com). Software controlled high power 10W blue LED array (http://www.led-tech.de) was used as light source for emission. A BG12 optical filter from Schott was placed in front of the LED array. A uniform distribution of the luminescence signal intensity with an adequate signal-to-noise- ratio signal was obtained within the plate region analyzed. Oxygen concentration was calculated using the Stern-Volmer equation (1).

$$\tau_0/\tau = 1 + K_{sv}\, pO_2 \tag{1}$$

τ_0 and τ are the luminescence lifetimes in the absence and presence of oxygen, respectively. The pO_2 is the partial pressure of oxygen. K_{sv} is the Stern-Volmer constant obtained by measuring τ_0 and τ_{air} under conditions of flushing the FFMR with pure nitrogen or air respectively.

Biocatalytic FFMR

If not mentioned otherwise, D-Ala was used as substrate. Alternative substrates were D-Met and a racemic mixture of D/L-Ala. Substrate concentration varied in the range 10 – 25 mM, as indicated. A 50 mM potassium phosphate buffer (pH 8.0) was used. Catalase (from bovine liver; Sigma-Aldrich) was optionally added to the buffer in a concentration of 0.1 mg/mL. Reactions were performed at 30 (± 1) °C applying variation in liquid and gas flow rates as well as in reactor inclination angle. Samples were collected from out-flow and analyzed. Enzymatic conversion was usually measured employing HPLC. Pyruvate, which is the product of transformation of D-Ala, was alternatively determined spectrophotometrically (AFLUOstar

Omega plate reader), measuring NADH consumption (at 340 nm) for pyruvate reduction by L-lactic acid dehydrogenase (from rabbit muscle; Sigma-Aldrich).

Assays and other analytical procedures

Protein of enzyme extract was routinely measured using Roti-Nanoquant and Roti-Quant assays (Carl Roth). Alternatively, Pierce protein assay was used for immobilization samples. Protein assays were calibrated against BSA. DAAO activity was measured spectrophotometrically using a reported peroxidase-coupled assay reported elsewhere (Bolivar and Nidetzky, 2012a). Horseradish peroxidase (type VI-A) from Sigma-Aldrich was used. D-Ala (10 mM) was applied as substrate. One activity unit is the enzyme amount producing 1 µmol H_2O_2/min under the conditions used (30 °C, pH 8.0).

Other methods

The following analytical methods used are described in the Supporting Information: confocal laser scanning microscopy, viscosity measurement, contact angle determination, and surface tension measurement.

Results and Discussion

FFMR operation, and flow regime characterization

Continuous gas-liquid phase contacting in a stably operated FFMR requires careful control of the pressures of the two phases, to avoid phase intermixing or dry-out of the liquid film. Therefore, interfacing of the basic FFMR to a suitable combination of in- and outflow pumps and also massflow meter-controlled air supply were crucial parameters of the final reactor set-up, as shown schematically in Figure 1. Figure S1 in the Supporting Information shows photographs of the reactor. FFMR geometry parameters are summarized in Table S1. Physical parameters of the gas and liquid phases used are shown in Table S2. Using confocal laser-scanning microscopy, we showed that the liquid-filled microchannels were completely wetted (Figure 2). The surface of the stagnant film under non-flowing conditions took the form of a shallow meniscus, where liquid is slightly pulled up along the sides of the channel as result of capillary forces and small channel width (Yeong et al., 2006). The effect enhances the specific gas-liquid surface area as compared to a completely flat surface profile. Figure S2 shows the confocal laser-scanning microscopy pictures of a dry microchannel plate for reference.

The liquid film is characterized by its thickness (δ_L) and volume (V_L). δ_L was calculated according to Nusselt's theory to vary between 47 and 102 µm for vertical operation of the reactor and depending on the Q_L used (Figure S3 and Eq S1, Supporting Information). The corresponding V_L varied in the range $1.5 - 1.7 \times 10^{-19}$ m^3 (Figure S3 and Eq S2). Existing correlations and equations (see the Supporting Information) were used to characterize hydrodynamic properties of the liquid film and its associated gas-liquid interface (Table 1, Figures S4 - S10 and the associated Eqs S3 - S15). The dimensionless liquid-side Reynolds number (Re_L) varied between 1 and 10, indicating a fully developed laminar liquid flow at all conditions used (Figure S5 and Eq S6). Because the gas-side Reynolds number (Re_G, Figure S6 and Eq S7) was also low (≤ 2.0), we exclude the possibility of turbulent wave formation on the liquid surface as result of Kelvin-Helmholtz instabilities. Tendency of a liquid film surface to change from hydrodynamically smooth (stratified flow) to laminar wavy character (wavy flow) depends on both the liquid flow rate Q_L and reactor inclination angle Θ (Figures S5, S8, and Eqs S11 - S13). Results of regime analysis based on empirical correlations (Supporting Information) suggest that the experimental conditions used (Q_L, Θ) involved transition from smooth to wavy gas-liquid interfaces (Table1, Figures S5 and S8). Figure 3 provides direct evidence of the occurrence of wavy flow based on measurements over time of the O_2 concentration at the outlet of the reactor. A summary of FFMR parameters is given in Table 1. To our knowledge, hydrodynamic characterization of an FFMR for O_2-dependent bioprocessing is described here for the first time.

Enzyme Immobilization in Microchannels

Upon hydration, the γ-aluminium oxide wash-coat layer of the microchannel walls will develop slightly acidic hydroxy groups on the surface. At pH 8.0, therefore, Z_{basic2}_*Tv*DAAO is expected to become attached to the partly anionic wall surfaces via its positively charged binding module. Immobilization was studied under liquid flow, recirculating the enzyme solution over the plate (Q_L range: 0.88 – 2.67 $mL\cdot min^{-1}$), or under static conditions, allowing the microchannel surface to become soaked with enzyme solution. Figure 4 shows the course of static immobilization of 0.75 oxidase units, resulting in about 0.60 units to become immobilized. Immobilization was relatively slow, requiring ≥3 h to be complete. About 20% of the initial activity was thus lost in the process. The same amount (0.6 units) of enzyme activity was immobilized "under flow". Q_L of 1.44 $mL\cdot min^{-1}$ (axial flow rate $u_L = 1.77 \times 10^{-2}\ m\cdot s^{-1}$; $Re_L = 1.35$) was optimal for the immobilization yield. It was possible to increase the unit amount/plate to about 1.1 on performing the immobilization a second time. Immobilizing more often than twice did not further enhance the units attached. The microchannel surface appeared to have become 73 % saturated thus and the amount of bound protein under these conditions corresponded to the estimated maximum binding capacity of the plate (1.52 units, equivalent to 0.026 mg protein), assuming monolayer adsorption of only the Z_{basic2} part of the fusion protein on the available microchannel surface (5 $mg\cdot m^{-2}$) (see Table S3 and Figure S11 for more details). It should be noted however that the calculation ignores the nanoporous structure of the wash-coat layer, which might increase the surface area available to the enzyme. No detachment of immobilized enzyme (measured as protein or oxidase activity released into solution) was observed under liquid flow at different Q_L using buffer or substrate solution. Assuming complete liquid filling of the microchannels, the total working volume was calculated (Eq S2) to be 0.19 mL. Accordingly, the volumetric reaction rate catalyzed by the immobilized oxidase would be 9.8 $\times 10^{-2}\ mM\cdot s^{-1}$.

Characterization of Gas-Liquid Oxygen Mass Transfer

A convenient but also somewhat insufficient approach of oxygen transfer rate determination (used herein for comparison purpose) is based on inline O_2 concentration measurements at reactor entrance and outlet. We developed a method for direct O_2 concentration measurement from within the microchannel plate at temporal and spatial resolution (Figures 5a and 6a). Because gas-liquid mass transfer could vary across L_C depending on the flow regime (e.g. under wavy flow) and there could exist spatial heterogeneity in O_2 supply to the microchannels, the capability of local internal O_2 concentration measurement presented significant advance for characterization of gas-liquid oxygen transfer in the FFMR.

Figure 5a shows results of an O_2 concentration "imaging" analysis from the immobilized oxidase microchannel plate operated under variable O_2 supply from the gas flow to the falling liquid film. Except for the most peripheral plate regions, the dissolved O_2 was almost homogeneously distributed across the whole plate area. Figure 5b shows the spatially averaged O_2 concentration measured internally under the different conditions used and compares it to the corresponding O_2 concentrations recorded in inflow and outflow (see also Figure S12 in Supporting Information). Under "gassing in" conditions the internal O_2 concentration was quickly brought to the maximum possible level of air saturation (measurements #7 - #10), indicating that the oxygen transfer rate outweighed by far the O_2 consumption rate by the immobilized enzyme. From these results, therefore, it would be only possible to state that the overall mass transfer coefficient K_La exceeds the inverse of the characteristic time of the enzymatic reaction, which in turn is given by the ratio of the maximum volumetric reaction rate (9.8×10^{-2} mM·s^{-1}) and the O_2 solubility (0.25 mM), hence is 0.392 s^{-1}

To enhance the internal O_2 consumption rate for oxygen transfer rate determination, glucose and soluble glucose oxidase from *Aspergillus niger* were added to the liquid phase. (Note: no catalase was present in these experiments.) Results of FFMR operation at variable O_2 supply are summarized in Figure 6. When gassing with air was used, the averaged internal O_2 concentration at steady state was about 60% of the air-saturated level. The internally measured

O_2 concentration did not vary with L_c and was independent of channel position on plate (Figure 5a). At steady state ($d[O_2]/dt = 0$), the overall mass transfer coefficient K_La was obtained from Equation 2 because the oxygen concentration gradient ($[O_2]^* - [O_2]$) and the oxygen consumption rate (r_O) by glucose oxidase were known. $[O_2]^*$ is the concentration at air saturation.

$$K_La\ ([O_2]^* - [O_2]) = r_O \qquad (2)$$

Using $r_O = 450\ \mu M \cdot s^{-1}$ a value of 7.5 (± 0.5) s^{-1} was calculated for K_La. The K_La values determined with the same FFMR for a variety of gas-liquid systems were all in a similar range of 3 - 8 s^{-1} (Illner et al., 2014; Kashid et al., 2011; Sobieszuk et al., 2012; Yeong et al., 2006; Yue et al., 2007). Measuring O_2 transfer into water, Illner et al. (2014) reported a K_La of 6 s^{-1}. It is worth noting in this context the limitation of a K_La determination based solely on O_2 concentration measurements in the in- and outflow, as used for example in the study of Illner et al. (2014). The method based on oxidation of glucose by soluble glucose oxidase cannot be used at all due to the complete deoxygenation of the liquid flowing into and out of the reactor. Application of the "gassing in" method where deoxygenated liquid is fed into the reactor and the O_2 concentration is measured in the outflow is limited in that the maximum K_La value measurable corresponds to the reciprocal residence time (Table 1; see also Illner et al., 2014). The K_La thus obtained is lower than the K_La determined from the experiment using soluble glucose oxidase and local O_2 concentration measurements. The liquid side mass transfer coefficient K_L was calculated using relationships from film theory (Equation 3) and penetration theory (Equation 4) recommended for flow regimes $Fo' > 1$ and $Fo' < 1$, respectively (Figure S10).

$$K_L = D_{eff}/\delta_L \qquad (3)$$

$$K_L = 2\ (u_L D_{eff}/\pi L_c)^{1/2} \qquad (4)$$

Using Eq 2 for the conditions of operation used in Figure 5, calculated K_L values were in the range 1.71 – 1.96 × 10^{-5} m·s^{-1} depending on δ_L varying between 65 and 82 µm. Using Eq 3, K_L values in the range 2.09 – 2.25 × 10^{-5} m·s^{-1} were obtained, again depending on δ_L. K_L values were also calculated for all the other conditions used for the FFMR operation, and they are summarized in Table 1 and some additional results are shown in Table S5. The K_L values thus obtained agree with literature on the basis of the same order of magnitude for falling liquid film reactor systems (Kashid et al., 2011; Schagen and Modigell, 2004; Sobieszuk et al., 2012; Yeong et al., 2004; Yue et al., 2007; Zhang et al., 2009), although the reported K_L values for microstructured falling liquid film systems are typically somewhat higher (≤ 4-fold) than the ones found here. For example, a minimum K_L value of 5.5 × 10^{-5} m·s^{-1} was obtained in the studies of (Sobieszuk et al., 2012; Zhang et al., 2009). Lowering of the film thickness under wavy flow as compared to stratified flow conditions (while the latter are generally assumed in the calculations) is one possible reason that the used correlations (Eqs 3 and 4) might underestimate the actual K_L. Side-wall shear stress in microchannels could also affect the K_L and is not accounted for in the correlations used (Sobieszuk et al., 2012; Zhang et al., 2009). Assuming again stratified flow conditions that involve a smooth gas-liquid interface, the specific gas-liquid area (a) was calculated from the reciprocal film thickness (Yeong et al., 2004). Values of a in the range 1.7 – 2.3 × 10^{4} m^{-1} were thus obtained. Therefore, this resulted in estimates of K_La in the range 0.34 – 0.45 s^{-1}, significantly lower than the K_La of 7.5 s^{-1} determined experimentally. Besides the K_L that may have been underestimated somewhat as discussed above, the actual specific surface area is also likely to have been higher than estimated (up to 1×10^{5} m^{-1}). Firstly, δ_L has been shown experimentally to be typically lower by 10 - 30 % than the calculated δ_L (Yeong et al., 2004; Yeong et al., 2006). According to the studies of Yeong et al. the effect on δ_L might be even more pronounced for a microchannel plate with comparably large channel dimensions, as used here (600 µm w_C and 200 µm d_C), and at low flow rates. Secondly, the curvature of the liquid surface (Figure 2) also affects the specific surface area. Yeong et al. (2006) show the trend that curvature, hence a, increases at low flow rates, and the effect is again more pronounced for the comparably wider microchannels. Thirdly, the presence of surface waves (Figure 3) causes the liquid film thickness δ_L and hence the diffusion path length to vary significantly between wave crest and trough. Therefore, the rate of gas-to-liquid O_2 transfer in the wavy flow regime depends on the reactor variables length and time. These effects can strongly influence the local mass transfer. Increases in local mass transfer by a factor of up to 3 compared to a conservatively estimated global mass transfer have been reported (Schagen and Modigell, 2004; Schagen and Modigell, 2007).

Biocatalytic transformation using the immobilized enzyme FFMR

Continuous oxidative deamination of D-Ala by immobilized Z_{basic2}_*Tv*DAAO was performed in the FFMR under variation of Q_L and Θ as the key process variables. Gas flow was constant. Figure S13 shows the reaction rate and product concentration expected for the operation of the reactor at 90 ° and at the complete range of liquid flows used. (Note: Figure S14 shows the composition of the product stream. Acetate was a major product of the reaction. Its formation was explained by uncatalyzed decarboxylation of the pyruvate in the presence of H_2O_2. On addition of soluble catalase (Figure S14), release of acetate was strongly decreased.) Figure 7a shows a time course of product formation that reveals stable reactor operation for at least 30 h. Because oxygen transfer was clearly not limiting the overall transformation rate (see Figures 5 and 6), the results imply a stable enzyme. The operational half-life time of the immobilized enzyme can only be roughly estimated from the data but it was 72 h or greater. For the 30h of operation time, the enzyme has been reused about 4×10^4 times as compared to reaction under the same conditions employing soluble enzyme.

Fast inactivation of DAAO on exposure to gas-liquid interfaces complicates use of the oxidase in bubble-areated reactors. In preventing surface-immobilized enzymes from being contacted with the gas-liquid interface, therefore, the FFMR succeeded in combining extremely efficient O_2 supply with proper protection of the enzyme catalyst used. That would be difficult to achieve in other apparatus (Kashid et al., 2011; Sobieszuk et al., 2012; Yue et al., 2007). Oriented immobilization of Z_{basic2}_*Tv*DAO onto FFMR plate is expected to provide stabilization compared with the free enzyme as result of the combination of protection against air bubble surfaces and protection against subunit dissociation (Bolivar and Nidetzky, 2012a). However, complete stabilization of the enzyme is not expected due to the absence of direct interactions between the enzyme and the anionic support, therefore gradual decrease of activity is consistent with findings related to the use of solid-supported *Tv*DAAO (Bolivar and Nidetzky, 2012a).

Figure 7 and Figure S14 show effects of varied Q_L (panel b) and Θ (panel c) on the residence time and product concentration released at steady state. Note: in consequence of δ_L being dependent on both Q_L and Θ, as shown in Eq S1, V_L changed on variation of either parameter, thus affecting also the residence time. Whereas change in V_L would affect in a well predictable fashion the product formation in a reaction involving a soluble catalyst, its influence on a heterogeneously catalyzed reaction is not equally clear, as follows. The variable V_L has the additional effect that it alters the degree to which the microchannel walls are wetted. Therefore, assuming a homogeneous deposition of the immobilized enzyme on the internal surface of the microchannels, incomplete channel wetting would result in a correspondingly incomplete use of the total amount of enzyme present. Substrate supply would take place to only a certain part of the catalytically active surface area. Therefore, this would result in an attenuated response of the product formation to residence time changes due to variation in Q_L; and it would also create a dependence of the product formation on Θ when the reactor is operated at constant Q_L. Figure 7b and 7c compares the measured product concentrations to concentrations calculated for conditions, in which the completeness of utilization of the immobilized enzyme depended on or was independent of Q_L. A scenario of Q_L and hence V_L dependent use of the immobilized enzyme was in excellent agreement with the experimental data and is therefore strongly supported. The results also suggest that the effective amount of immobilized enzyme activity (*Cat* in the legend of Figure 7) was correctly determined from the simple balance between the enzyme activity in solution before and after the immobilization. This in turn implies that Z_{basic2}_*Tv*DAAO retained most ($\geq$ 80% within limits of error) of its biological activity in solution after the immobilization on the microchannel walls. The concept of oriented enzyme immobilization via the Z_{basic2} module is therefore supported.

Conclusions

We report integrated development and detailed characterization of an advanced FFMR for O_2-dependent chemical transformations with immobilized enzymes. Reversible, selective and oriented protein immobilization was achieved through concurrent designs of the microchannel surface (γ-Al_2O_3 wash-coat layer) and enzyme used (Z_{basic2} fusion protein). This approach of enzyme immobilization might be applicable broadly. Method of internal O_2 concentration measurement was developed and shown to be useful for determination of parameters of the gas-liquid O_2 transfer. Reactor performance dependent on Q_L and Θ was analyzed and explained/modeled in terms of only partial use of the immobilized enzyme due to incomplete wetting of microchannel walls at low V_L. The immobilized enzyme FFMR offers extremely efficient O_2 supply to the biocatalytic reaction in a manner protecting the enzymes against interfacial inactivation. The classical bubble aeration often creates severe problems of enzyme stability, especially when soluble or surface-exposed immobilized enzymes are used. Enzymes immobilized in the pores of solid carriers are protected effectively but the enhanced stability is often traded off against a severely reduced activity due to diffusional limitations. Besides its use for enzymatic reaction characterization, including the determination of intrinsic kinetics and the optimization of reaction conditions, the FFMR is also useful for production. Scale out or scale up of the FFMR's production capacity has been demonstrated for chemical syntheses (Pennemann et al., 2004) and the resulting experience should be transferable in principle to biocatalytic O_2-dependent transformations. However, to make fully use of the FFMR's high-performance oxygenation capabilities for the purpose of production, the immobilization needs to be improved regarding the activity amount loadable on the microchannel surface. Thus, high substrate conversions could be reached in the relative short residence times (seconds range) available to this reactor type. By applying suitable scale-up strategies (e.g. increase of size and length of microchannels) (Illner et al., 2014; Pennemann et al., 2004), residence time and conversion might also be enhanced substantially. Finally, we note that O_2-dependent biotransformations are often carried out by using whole cells preferably as compared to isolated enzymes (Karande et al., 2016). Although the immobilization will probably be not the same when whole cells are used, the FFMR might still present an interesting reactor solution for, and is extendable in principle to, O_2-dependent conversions catalyzed by whole cell systems.

Acknowledgements

We thank Dr. Christoph Neubauer (RCPE GmbH, Austria) for assisting the contact angle measurements; Dr. Heimo Wolinski (Institute of Molecular Biosciences, University of Graz) for help with confocal laser-scanning microscopic analysis; and Dr. Sergey Borisov (Institute of Analytical and Food Chemistry, Graz University of Technology) for providing colored nanoparticles.

References

Bolivar JM, Wiesbauer J, Nidetzky B. 2011. Biotransformations in microstructured reactors: More than flowing with the stream? Trends Biotechnol 29:333–342.

Bolivar JM, Nidetzky B. 2012a. Oriented and selective enzyme immobilization on functionalized silica carrier using the cationic binding module Z basic2: design of a heterogeneous D-amino acid oxidase catalyst on porous glass. Biotechnol Bioeng 109:1490–1498.

Bolivar JM, Nidetzky B. 2012b. Positively charged mini-protein Zbasic2 as a highly efficient silica binding module: opportunities for enzyme immobilization on unmodified silica supports. Langmuir 28:10040–10049.

Bolivar JM, Nidetzky B. 2013. Multiphase biotransformations in microstructured reactors: opportunities for biocatalytic process intensification and smart flow processing. Green Process Synth 2: 541-559.

Bolivar JM, Schelch S, Mayr T, Nidetzky B. 2015. Mesoporous silica materials labeled for optical oxygen sensing and their application to development of a silica-supported oxidoreductase biocatalyst. ACS Catal 5:5984–5993.

Commenge J-M, Obein T, Framboisier X, Rode S, Pitiot P, Matlosz M. 2011. Gas-phase mass-transfer measurements in a falling-film microreactor. Chem Eng Sci 66:1212–1218.

Commenge J-M, Obein T, Genin G, Framboisier X, Rode S, Schanen V, Pitiot P, Matlosz M. 2006. Gas-phase residence time distribution in a falling-film microreactor. Chem Eng Sci 61:597–604.

Dencic I, Hessel V, de Croon MHJM, Meuldijk J, van der Doelen CWJ, Koch K. 2012. Recent changes in patenting behavior in microprocess technology and its possible use for gas-liquid reactions and the oxidation of glucose. ChemSusChem 5:232–245.

Dencic I, Meuldijk J, de Croon M, Hessel V. 2011. From a review of noble metal versus enzyme catalysts for glucose oxidation under conventional conditions towards a process design analysis for continuous-flow operation. J Flow Chem 1:13–23.

Fercher A, Borisov SM, Zhdanov AV, Klimant I, Papkovsky DB. 2011. Intracellular O2 sensing probe based on cell-penetrating phosphorescent nanoparticles. ACS Nano 5:5499–5508.

Fernandes P. 2010. Miniaturization in biocatalysis. Int J Mol Sci 11:858–879.

Garcia-Ochoa F, Gomez E. 2009. Bioreactor scale-up and oxygen transfer rate in microbial processes: an overview. Biotechnol Adv 27:153–176.

Gemoets HPL, Su Y, Shang M, Hessel V, Luque R, Noël T. 2016. Liquid phase oxidation chemistry in continuous-flow microreactors. Chem Soc Rev *45:83–117.*

Günther A, Jensen KF. 2006. Multiphase microfluidics: From flow characteristics to chemical and materials synthesis. Lab Chip - Miniaturisation Chem Bio 6:1487–1503.

Gutmann B, Cantillo D, Kappe CO. 2015. Continuous-flow technology-a tool for the safe manufacturing of active pharmaceutical ingredients. Angew Chem Int Ed 54:6688–6728.

Hall M, Bommarius AS. 2011. Enantioenriched compounds via enzyme-catalyzed redox reactions. Chem Rev 111:4088–4110.

Hartman RL, Jensen KF. 2009. Microchemical systems for continuous-flow synthesis. Lab Chip - Miniaturisation Chem Biol 9:2495–2507.

Hessel V, Angeli P, Gavriilidis A, Löwe H. 2005. Gas-liquid and gas-liquid-solid microstructured reactors: Contacting principles and applications. Ind Eng Chem Res 44:9750–9769.

Hessel V, Tibhe J, Noël T, Wang Q. 2014. Biotechnical micro-flow processing at the EDGE – lessons to be learnt for a young Discipline. Chem Biochem Eng Q J 28:167–188.

Hollmann F, Arends IWCE, Buehler K, Schallmey A, Bühler B. 2011. Enzyme-mediated oxidations for the chemist. Green Chem 13:226.

Illner S, Hofmann C, Löb P, Kragl U. 2014. A falling-film microreactor for enzymatic oxidation of glucose. ChemCatChem 6:1748–1754.

Jähnisch K, Hessel V, Löwe H, Baerns M. 2004. chemistry in microstructured reactors. Angew Chem Int Ed 43:406–446.

Karande R, Schmid A, Buehler K. 2016. Applications of Multiphasic Microreactors for Biocatalytic Reactions. Org Process Res Dev In press: DOI: 10.1021/acs.oprd.5b00352

Kashid MN, Renken A, Kiwi-Minsker L. 2011. Gas–liquid and liquid–liquid mass transfer in microstructured reactors. Chem Eng Sci 66:3876–3897.

Kashid MN, Kiwi-Minsker L. 2009. Microstructured reactors for multiphase reactions: State of the art. Ind Eng Chem Res 48:6465–6485.

Kawakami K, Kawasaki K, Shiraishi F, Kusunoki K. 1989a. Performance of a honeycomb monolith bioreactor in a gas-liquid-solid three-phase system. Ind Eng Chem Res 28:394–400.

Kawakami K, Adachi K, Minemura N, Kusunoki K. 1989b. Characteristics of a gas-liquid-solid, three-phase, honey-comb-monolith bioreactor. Oxidation of glucose by immobilized glucose oxidase. Int Chem Eng 29:320–327.

Lundemo MT, Woodley JM. 2015. Guidelines for development and implementation of biocatalytic P450 processes. Appl Microbiol Biotechnol 99:2465–2483.

Mallat T, Baiker A. 2004. Oxidation of alcohols with molecular oxygen on solid catalysts. Chem Rev 104:3037–3058.

Mhiri N, Monnier H, Falk L. 2011. Intensification of the G/L absorption in microstructured falling film application to the treatment of chlorinated VOC’s. Part III: Influence of gas thickness channel on mass transfer. Chem Eng Sci 66:5989–6001.

Monnier H, Falk L, Lapicque F, Hadjoudj R, Roizard C. 2010. Intensification of G/L absorption in microstructured falling film. Application to the treatment of chlorinated VOC’s – part I: Comparison between structured and microstructured packings in absorption devices. Chem Eng Sci 65:6425–6434.

Monnier H, Falk L. 2011. Intensification of G/L absorption in microstructured falling film. Application to the treatment of chlorinated VOC’s - part II: Modeling and geometric optimization. Chem Eng Sci 66:2475–2490.

Monti D, Ottolina G, Carrea G, Riva S. 2011. Redox reactions catalyzed by isolated enzymes. Chem Rev 111:4111–4140.

Moser C, Mayr T, Klimant I. 2006. Microsphere sedimentation arrays for multiplexed bioanalytics. Anal Chim Acta 558:102–109.

Podgoršek A, Zupan M, Iskra J. 2009. Oxidative Halogenation with “Green” Oxidants: Oxygen and Hydrogen Peroxide. Angew Chem Int Ed 48:8424–8450.

Punniyamurthy T, Velusamy S, Iqbal J. 2005. Recent advances in transition metal catalyzed oxidation of organic substrates with molecular oxygen. Chem Rev 105:2329–2363.

Que L, Tolman WB. 2008. Biologically inspired oxidation catalysis. Nature 455:333–340.

Rebrov EV, Duisters T, Löb P, Meuldijk J, Hessel V. 2012. Enhancement of the liquid-side mass transfer in a falling film catalytic microreactor by in-channel mixing structures. Ind Eng Chem Res 51:8719–8725.

Schagen A, Modigell M. 2004. Luminescence technique for the measurement of local concentration distribution in thin liquid films. Exp Fluids 38:174–184.

Schagen A, Modigell M. 2007. Local film thickness and temperature distribution measurement in wavy liquid films with a laser-induced luminescence technique. Exp Fluids 43:209–221.

Sheldon RA, Arends IWCE, Brink GJT, Dijksman A. 2002. Green, catalytic oxidations of alcohols. Acc Chem Res 35:774–781.

Sheldon RA. 2015. Recent advances in green catalytic oxidations of alcohols in aqueous media. Catal Today 247:4–13.

Shi Z, Zhang C, Tang C, Jiao N. 2012. Recent advances in transition-metal catalyzed reactions using molecular oxygen as the oxidant. Chem Soc Rev 41:3381–3430.

Sobieszuk P, Aubin J, Pohorecki R. 2012. Hydrodynamics and mass transfer in gas-liquid flows in microreactors. Chem Eng Technol 35:1346–1358.

Tomaszewski B, Lloyd RC, Warr AJ, Buehler K, Schmid A. 2014a. Regioselective biocatalytic aromatic hydroxylation in a gas-liquid multiphase tube-in-tube reactor. ChemCatChem 6:2567–2576.

Tomaszewski B, Schmid A, Buehler K. 2014b. Biocatalytic production of catechols using a high pressure tube-in-tube segmented flow microreactor. Org Process Res Dev 18:1516–1526.

Tufvesson P, Lima-Ramos J, Haque NA, Gernaey KV, Woodley JM. 2013. Advances in the process development of biocatalytic processes Org Process Res. Dev 17:1233–1238.

Turner NJ. 2011. Enantioselective oxidation of C-O and C-N bonds using oxidases. Chem Rev 111:4073–4087.

Wiesbauer J, Bolivar JM, Mueller M, Schiller M, Nidetzky B. 2011. Oriented Immobilization of enzymes made fit for applied biocatalysis: Non-covalent attachment to anionic supports using Zbasic2 module. ChemCatChem 3:1299–1303.

Wohlgemuth R, Plazl I, Žnidaršič-Plazl P, Gernaey KV, Woodley JM. 2015. Microscale technology and biocatalytic processes: opportunities and challenges for synthesis. Trends Biotechnol 33:302–314.

Woodley JM. 2006. Microbial biocatalytic processes and their development. Adv Appl Microbiol 60:1–15.

Yeong KK, Gavriilidis A, Zapf R, Kost H-J, Hessel V, Boyde A. 2006. Characterisation of liquid film in a microstructured falling film reactor using laser scanning confocal microscopy. Exp Therm Fluid Sci 30:463–472.

Yeong KK, Gavriilidis A, Zapf R, Hessel V. 2004. Experimental studies of nitrobenzene hydrogenation in a microstructured falling film reactor. Chem Eng Sci 59:3491–3494.

Yue J, Chen G, Yuan Q, Luo L, Gonthier Y. 2007. Hydrodynamics and mass transfer characteristics in gas–liquid flow through a rectangular microchannel. Chem Eng Sci 62:2096–2108.

Zanfir M, Gavriilidis A, Wille C, Hessel V. 2005. Carbon dioxide absorption in a falling film microstructured reactor: Experiments and modeling. Ind Eng Chem Res 44:1742–1751.

Zhang H, Chen G, Yue J, Yuan Q. 2009. Hydrodynamics and mass transfer of gas-liquid flow in a falling film microreactor. AIChE J 55:1110–1120.

List of symbols

A: cross-sectional area of the liquid phase, m^2

Cat: enzyme activity deposited on the FFMR plate, $mol \cdot s^{-1}$

d_C: depth of liquid channel, µm

D_{eff}: diffusion coefficient of O_2, $m^2 \cdot s^{-1}$

Fo': modified mass Fourier number.

K_L: liquid side mass transfer coefficient, $m \cdot s^{-1}$

K_La: volumetric mass transfer coefficient, s^{-1}

K_{SV}: Stern-Volmer constant, hPa^{-1}

L_c: channel length, cm

P: product concentration, mM

pO_2: partial pressure of oxygen, hPa

Q_G: gas flow rate, $L \cdot h^{-1}$

Q_L: liquid flow rate, $m^3 \cdot s^{-1}$

Re_G: gas-side Reynolds number

Re_L: liquid-side Reynolds number

u_L: axial flow rate, $m \cdot s^{-1}$

V_L: liquid volume, mL

w_C: microchannel width, µm

w_G: gas chamber width, mm

δ_G: gas channel thickness, mm

δ_L: liquid film thickness, µm

Θ: reactor inclination angle, º

τ: luminescence lifetime, µs

τ_{air}: τ at air saturation, µs

τ_0: τ under deoxygenated conditions, µs

Figures captions

Figure 1. The flow chart of the FFMR system used in this study is shown. The system comprised besides the actual FFMR, a mass flow controller for gas delivery, two pumps controlling liquid in- and outflow, a water-bath for temperature control via the heat exchanger of the FFMR, and flow-through O_2 sensors at the inlet and the outlet of the liquid flow. Luminescence lifetime imaging was integrated to measure the O_2 concentration in proximity of the surface of the microchannels.

Figure 2. Confocal laser-scanning microscopic images of the microchannel plate are shown. The region of interest comprises details of one channel and parts of two adjacent channels of a wetted plate. The scale bars indicate 600 µm. a) 3D projection of Z-stack images; b) Z-projection of Z-stack images; c) orthogonal view of Z-stack images.

Figure 3. Oxygen concentrations in inlet and outlet are shown during operation of the FFMR containing immobilized Z_{basic2}_*Tv*DAAO (1.1 units). Figure shows time-resolved O_2 concentration measurements in the liquid stream at reactor inlet and outlet, obtained under conditions where the combination of variable Q_L and Θ used was favoring a hydrodynamically smooth or a laminar wavy surface. The O_2 concentration at reactor inlet was constant over time, and measurements exhibited little noise and O_2 saturation. Values for a Q_L of 1.60×10^{-8} m s^{-1} and a low Θ of 30° are shown. At the low Q_L (0.80×10^{-8} m s^{-1}) when Θ was 90°, the O_2 concentration at reactor outlet was also constant. Operating the reactor at an elevated Q_L (1.60×10^{-8} m s^{-1}) when Θ was low (30°) resulted in the onset of periodic up and down displacements of the O_2 concentration, eventually creating a sinusoidal wave-like time course of the dissolved O_2 in the outflow at steady state. Perturbation of the initially smooth interface appears to have

caused the effect, and the outflow O_2 concentration is thought to present a negative of the waving film thickness at reactor exit.

Figure 4. Time course of immobilization of Z_{basic2}_*Tv*DAAO on the microchannel plate is shown. Loss of activity in the supernatant during “static” immobilization is shown. A control (blank) is also shown which indicates that the enzyme ($0.15\ U\cdot mL^{-1}$) was stable in solution in the timespan of the immobilization experiment.

Figure 5. Results of internal and external O_2 concentration measurements during operation of the FFMR containing immobilized Z_{basic2}_*Tv*DAAO (1.1 units) are shown. The reactor was operated at $1.97 \times 10^{-8}\ m^3\cdot s^{-1}$ of liquid flow (25 mM D-Ala) and 45 º of reactor inclination angle Θ. Panel a shows the local O_2 concentration on the plate in hPa (1 hPa is equivalent to 1.16 µM at 30ºC). The region of interest for measurement comprises a rectangle of 14.8 mm × 23.5 mm located at the lower end of the plate, as indicated in the image #1 of panel a. Panel b shows O_2 concentration measurements with the flow-through sensors at reactor entrance and exit and compares these measurements to results of on-plate O_2 concentration measurements. Numbering is used to identify images from the upper panel that correspond to the local O_2 concentrations shown in the lower panel. In the first phase of the experiment (#2 - #3), the FFMR was operated with nitrogen flow, resulting in a complete deoxygenation of the plate. When air flow was switched on to 0.33 L/h (#3 - #8), the local O_2 concentration increased sharply, revealing a highly effective O_2 supply from the gas phase to the liquid phase. Eventually, air saturation was reached despite consumption of O_2 for the enzymatic reaction (#9 - #10). Deoxygenation was only possible when air was again replaced by N_2 (#11 - #12). Note that the connection between reactor and outflow sensor was not completely leak-proof for O_2 and therefore the O_2 concentration in outflow was higher than the one locally measured.

Figure 6. Results of internal O_2 concentration measurements during operation of the FFMR using soluble glucose oxidase (75 U/mL) are shown. Besides the enzyme, the liquid flow contained 100 mM D-glucose. The experiment was otherwise conducted as described in the legend of Figure 4. Panel a shows the local O_2 concentration on the plate in hPa (1 hPa is equivalent to 1.16 µM at 30ºC). Panel b shows average on-plate O_2 concentration measurements. Numbering is used to identify images from the upper panel that correspond to the local O_2 concentrations shown in the lower panel. Note that due to rapid consumption of O_2 by enzymatic reaction in solution, the O_2 concentration measured in the liquid flow at reactor entrance and exit was effectively zero. Setting the airflow to 0.33 L/h, the measured O_2 concentration on the microchannel plate corresponded to approximately 60% of the air-saturated level (gray line), indicated by measurements #1 - #3. On switching off the airflow and keeping the gas ports tightly closed, the internal O_2 concentration gradually decreased (measurement #4). Changing to N_2 flow resulted in complete deoxygenation of the plate (measurement #5). Opening up the gas ports to enable air to enter in the absence of controlled gas flow, the internal O_2 concentration increased again (measurements #6 - #8). An extremely high oxygenation capacity of the FFMR is demonstrated.

Figure 7. The total product concentration released on oxidation of D-Ala in the FFMR containing immobilized Z_{basic2}_*Tv*DAAO (1.1 units) is shown. The substrate concentration was 25 mM D-Ala. A time course of conversion is shown in panel *a* ($Q_L = 3.21 \times 10^{-8}\ m^3 \cdot s^{-1}$, $\Theta = 45^o$, $Q_G = 1.0$ L/h). The reactor was also operated at variable liquid flow (panel *b*, $\Theta = 30^o$) and inclination angle (panel *c*, $Q_L = 0.98 \times 10^{-8}\ m^3 \cdot s^{-1}$) and molar product concentrations at apparent steady state are shown. Assuming ideal plug flow of the liquid phase, performance of the reactor at steady state was modeled, expressing the product concentration *P* with the relationship, *P* =

$(AL_c/Q_L)(Cat/V_L)$, where A is the cross-sectional area of the liquid phase (m^2) and Cat is the enzyme activity used in the reaction (1.83×10^{-8} mol·s^{-1}). Note: Cat is the amount of activity immobilized on the microplate. Like V_L, A is dependent on Q_L and Θ. Now, the degree of wetting of the microchannel walls depends on V_L, hence A. In the case that immobilized enzyme is distributed homogeneously on the wall surface, the degree of channel wetting determines to which extent the immobilized enzyme is utilized under given reaction conditions, that is, the effectively used Cat_eff $(Q_L, \Theta) \leq Cat$. In the modeling it was assumed that the degree of wetting (V_L/V_L_max) determines the degree of Cat use, hence Cat_eff $(Q_L, \Theta) = CatV_L/V_L\_max$. V_L_max is the maximum liquid volume of the microchannels. Therefore, the dependence of Cat_eff on Q_L attenuates the effect of Q_L on P at constant Θ (panel *b*). Moreover, P becomes dependent on Θ under these conditions (panel *c*). The alternative scenario considered was that of Cat not being dependent on Q_L and Θ, as would be the case if all of the enzymes were immobilized at the bottom surface of the microchannel. Therefore, this leads to an inverse dependence of P on Q_L at constant Θ; and to a P independent of Θ at constant Q_L.

Table 1. Summary of FFMR operation parameters

Operation conditions	δ_L, µm	V_L, µL	Re_L	Residence time, s
Θ, 30°; Q_L, 0.82–8.50 × 10^{-8} $m^3 \cdot s^{-1}$	58–128	56–123	2.0–19.0	1.4–6.9
Θ, 45°; Q_L, 1.60–4.00 × 10^{-8} $m^3 \cdot s^{-1}$	65–89	63–85	2.8–6.7	2.1–3.9
Θ, 90°; Q_L 0.82–8.50× 10^{-8} $m^3 \cdot s^{-1}$	47–102	45-98	1.0–9.8	1.1–5.4
Θ, 5–90°; Q_L 0.98× 10^{-8} $m^3 \cdot s^{-1}$	50–112	48-107	1.2–12.6	4.8–10.9

Figure 1

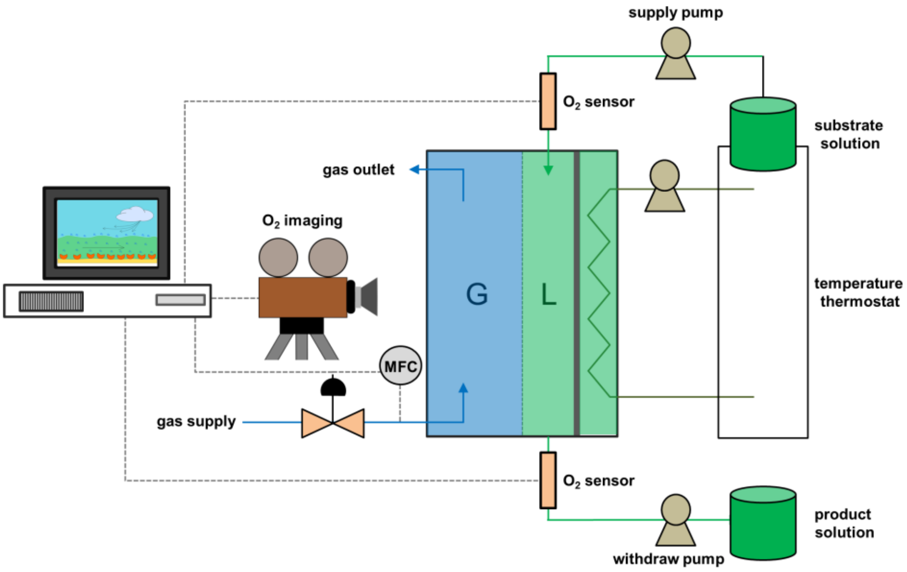
supply pump
O_2 sensor
substrate solution
gas outlet
O_2 imaging
G
L
temperature thermostat
MFC
gas supply
O_2 sensor
product solution
withdraw pump

Figure 2

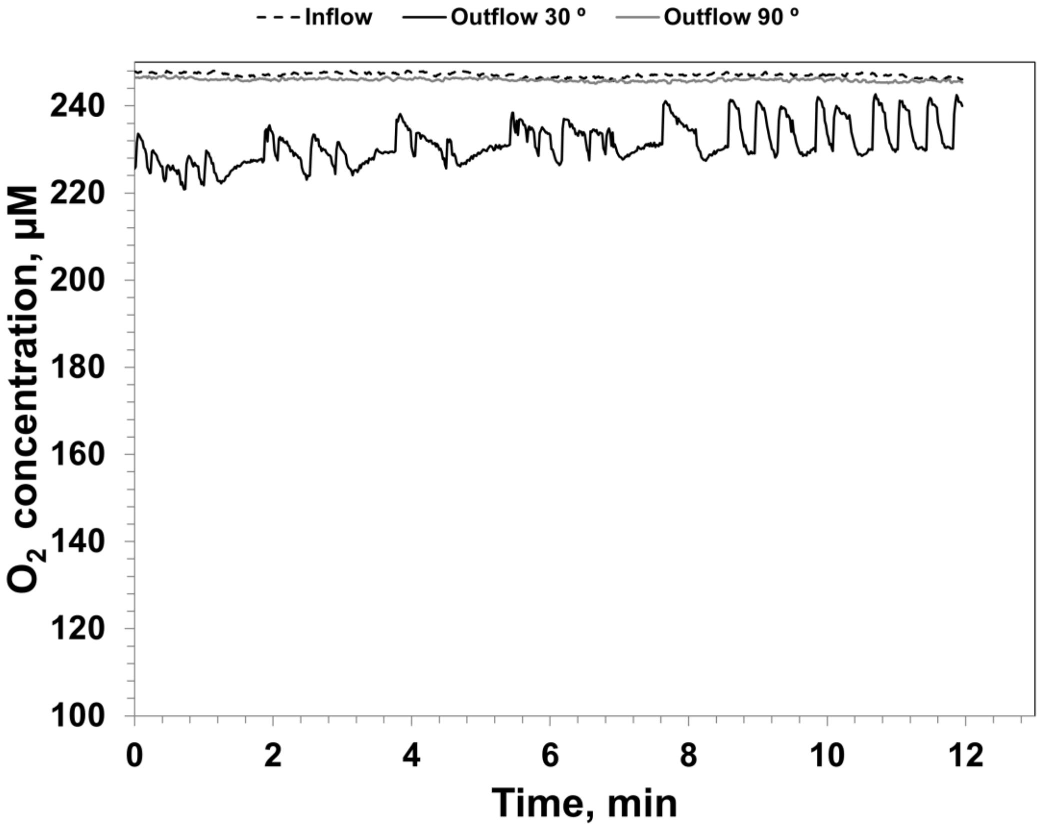

Inflow
Outflow 30 º
Outflow 90 º
O_2 concentration, µM
240
220
200
180
160
140
120
100
0
2
4
6
8
10
12
Time, min

Figure 4

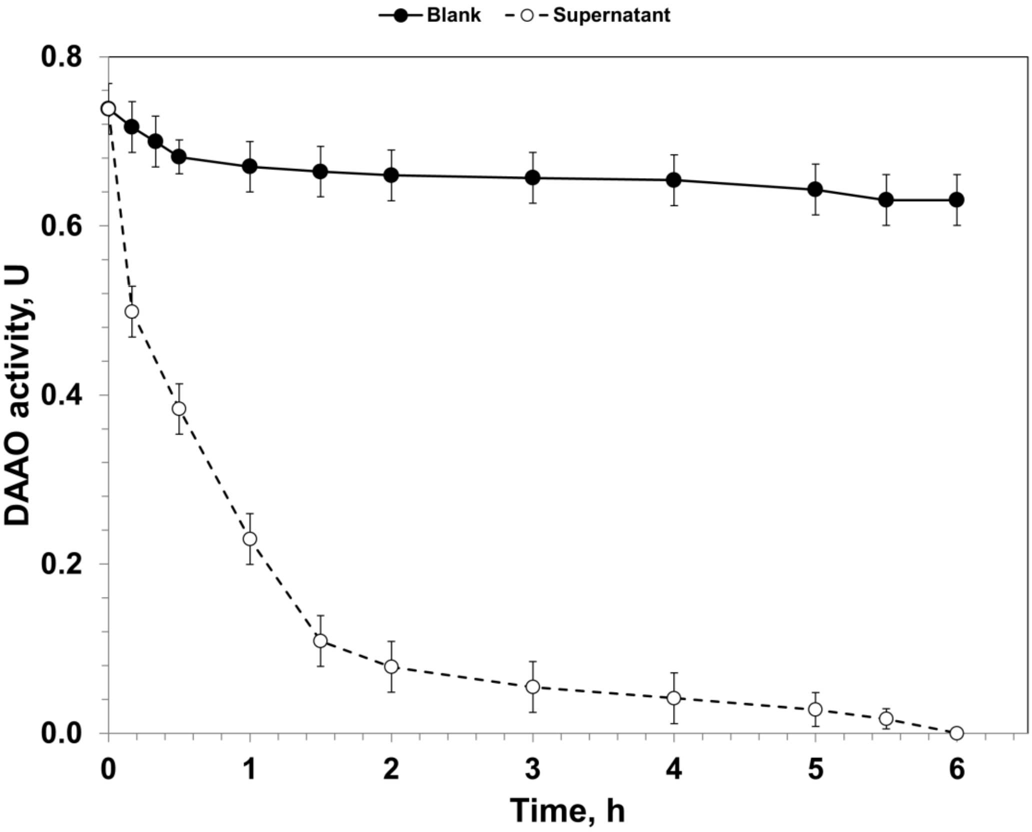
Blank
Supernatant
0.8
0.6
0.4
0.2
0.0
DAAO activity, U
0
1
2
3
4
5
6
Time, h

Figure 5

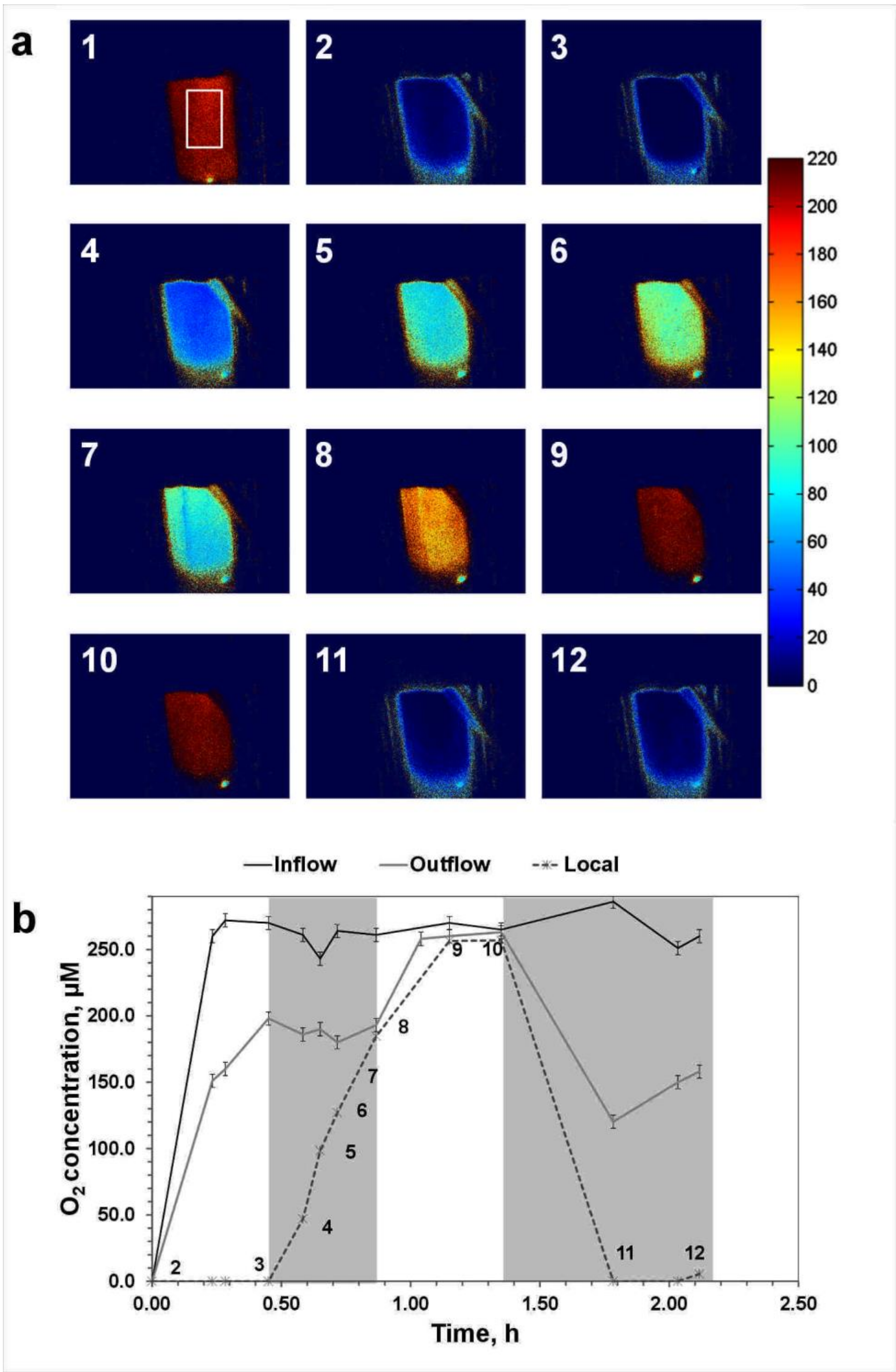
a
1
2
3
4
5
6
7
8
9
10
11
12
220
200
180
160
140
120
100
80
60
40
20
0
Inflow
Outflow
Local
b
O$_2$ concentration, μM
250.0
200.0
150.0
100.0
50.0
0.0
0.00
0.50
1.00
1.50
2.00
2.50
Time, h
2
3
4
5
6
7
8
9
10
11
12

Figure 6

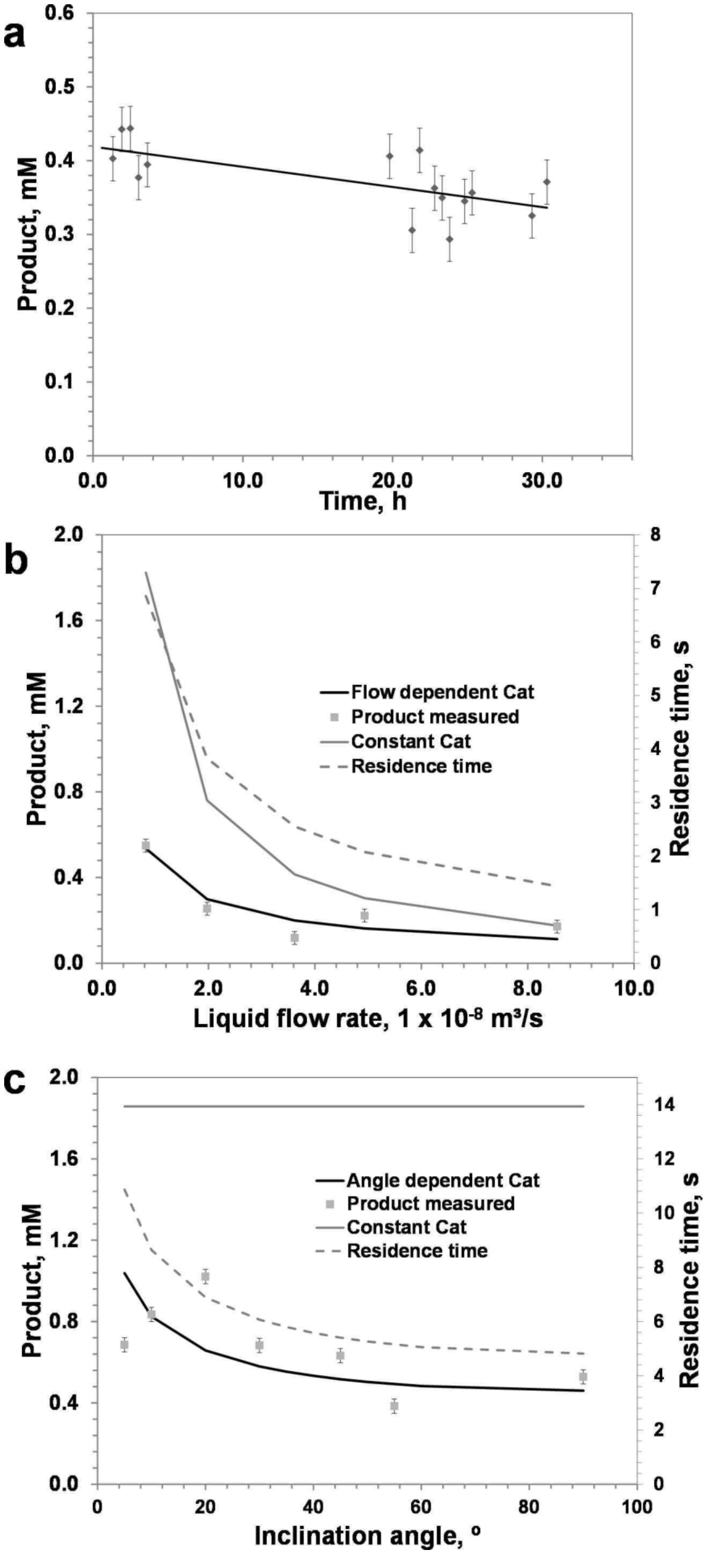
a
Product, mM
0.6
0.5
0.4
0.3
0.2
0.1
0.0
0.0
10.0
20.0
30.0
Time, h
b
Product, mM
2.0
1.6
1.2
0.8
0.4
0.0
Residence time, s
8
7
6
5
4
3
2
1
0
0.0
2.0
4.0
6.0
8.0
10.0
Liquid flow rate, 1 x 10-8 m³/s
Flow dependent Cat
Product measured
Constant Cat
Residence time
c
Product, mM
2.0
1.6
1.2
0.8
0.4
0.0
Residence time, s
14
12
10
8
6
4
2
0
0
20
40
60
80
100
Inclination angle, º
Angle dependent Cat
Product measured
Constant Cat
Residence time

SUPPORTING INFORMATION

Development of a fully integrated falling film microreactor for gas-liquid-solid biotransformation with surface immobilized O_2-dependent enzyme

Juan M. Bolivar[1], Christina E. M. Krämer[1], Birgit Ungerböck[2], Torsten Mayr[2], and Bernd Nidetzky[1,3*]

[1] Institute of Biotechnology and Biochemical Engineering, Graz University of Technology, NAWI Graz, Petersgasse 12, A-8010 Graz, Austria

[2] Institute of Analytical and Food Chemistry, Graz University of Technology, Stremayrgasse 16, A-8010 Graz, Austria

[3] Austrian Centre of Industrial Biotechnology, Petersgasse 14, A-8010 Graz, Austria

* Corresponding author

Phone: +43 316 873 8400; fax: +43 316 873 8434; e-mail: bernd.nidetzky@tugraz.at

S1. Supporting Methods

S1.1 Local Oxygen Concentration Measurement

Eudragit RL-100 nanoparticles were attached onto the □-Al_2O_3 layered surface of the microchannels by ionic adsorption. The utility of this procedure for immobilization of the nanoparticles was evaluated. It was important to show that the nanoparticles are distributed over the surface of the microchannels in a reasonably homogeneous fashion and that they are not washed away under conditions of flow. A test of stability of immobilized nanoparticles under liquid flow was therefore performed. Moreover, a procedure for the co-immobilization of the nanoparticles and the enzymes was developed. Colored Eudragit RL-100 nanoparticles were kindly provided by S. M. Borisov (Institute of Analytical Chemistry and Food Chemistry, Graz University of Technology). It was proven by visual inspection and also by photometric measurement of the liquid at outflow that Eudragit RL-100 nanoparticles were attached to the channel wall surface strongly enough so that they were not removed by the liquid flow in the range of flow rates used in the following experiments. For co-immobilization of the nanoparticles and the enzymes, continuous flow or static conditions were applied. The enzyme solution used for immobilization was shown to detach the previously adsorbed nanoparticles from the microchannel walls so that they agglomerated downstream of the channels. Therefore, Z_{basic2}_*Tv*DAAO was immobilized on the reaction plate first and immobilization of the nanoparticles was only done afterwards. Only a minor loss of Z_{basic2}_*Tv*DAAO activity was found (<10%) to occur in consequence of the additional immobilization of the nanoparticles. No detachment of the Eudragit RL-100 particles or the enzymes was detected under the application of liquid flow.

S 1.2 Other Methods

Confocal laser scanning microscopy images were collected with a model SP5 Leica Microsystems microscope. Self-luminescence of γ-Al_2O_3 (Nourmohammadi et al., 2012) and reflection (Yeong et al., 2006) were used for the collection of images. The emission bandwith was set in the range 499 – 624 nm. Data were analyzed with Fiji-ImageJ and visualized with IrfanView. Samples from enzymatic conversions were analyzed by HPLC. An Agilent 1200 system equipped with a 1290 Infinity autosampler HiP-ALS G1367B was used. A Merck Chromolith Performance RP-18e column was used, and elution was with 4 mM tetrabutylammonium phosphate in 50 mM potassium phosphate buffer (pH 7.0) at a flow rate of 2 mL/min. Before analysis, protein was removed by precipitation with perchloric acid (50 µL/mL sample; Polson et al., 2003) and the sample pH was re-adjusted to neutral with KOH. The kinematic viscosity of aqueous solutions was determined with a KPG-Viscosimeter according to Ostwald (Schott GmbH, Germany) at an operating temperature of 30 °C. The density measurement was done with a 5 mL pycnometer (Carl Roth GmbH, Germany) gravimetrically. The pycnometer and its content were at a constant temperature of 30 °C. Surface tension (σ_L) and contact angle (θ) were measured with an Easy Drop instrument (Krüss GmbH, Germany).

S2. Liquid and gas phase characterization

The liquid film thickness (δ_L) and the corresponding liquid volume (V_L) are described with equation S1 and S2 and they are shown in Figure S3, where Q_L is the liquid flow, ν_L and ρ_L are the kinematic viscosity and the density of the liquid phase, respectively, and g is the gravitational acceleration. The channel geometry is described by n_C, W_C, L_C (channel number, channel width, channel length). The equation used to calculate δ_L is following Nusselt's theory of 1916 (Commenge et al., 2011; Schagen and Modigell, 2004; Zanfir et al., 2005). Interfacial area (a) is calculated by equation S3.

$$\delta_L = \sqrt[3]{\frac{3Q_L\nu_L}{n_c w_c g\, sin(\Theta)}} \tag{S1}$$

$$V_L = {}^{2}\!/_{3}\, n_C w_C \delta_L L_c \tag{S2}$$

The gravity driven liquid phase is characterized by mean velocity (u_L, Figure S4 and Eq S4), superficial velocity at interphase (u, Figure S4 and Eq S5), liquid side Reynolds number (Re_L,

Figure S5 and Eq S6), where $d_{H,L}$ is the hydraulic diameter of the liquid phase, equation S7. Re_L describes the ratio of inertia to viscous forces of liquid phase and ratio of inertial forces to gravitational driving forces of the fluid, for Re_L numbers encountered in this study ($Re_L \leq 10$), liquid flow is considered to be fully developed laminar (Commenge et al., 2006; Commenge et al., 2011; Mhiri et al., 2011; Monnier et al., 2010; Monnier and Falk, 2011; Zanfir et al., 2005).

$$a = \frac{3}{2\,\delta_L} \tag{S3}$$

$$\bar{u}_L = \frac{\rho_L g \delta_L^2}{3\mu_L} sin(\Theta) \tag{S4}$$

$$u_L = \frac{\rho_L g \delta_L^2}{2\mu_L} sin(\Theta) \tag{S5}$$

$$Re_L = \frac{\rho_L \bar{u}_L d_{H,L}}{\mu_L} \tag{S6}$$

$$d_{H,L} = \frac{2\,w_C \delta_L}{w_C + \delta_L} \tag{S7}$$

The pressure driven stream of compressed air was characterized by the gas side Reynolds number (Re_G, Figure S6 and Eq S8), the mean velocity of the streaming air (u_G, Figure S7 and Eq S9) and the hydraulic diameter ($d_{H,G}$, Eq S10). Ω_G is the cross-sectional area of the gas phase, w_G is the gas chamber width, and δ_G is the gas channel thickness. The geometric parameters needed to determine the gas side hydraulic diameter $d_{H,G}$ are given previously in Table 1 (Commenge et al., 2011; Mhiri et al., 2011; Monnier and Falk, 2011). Air density (ρ_G, 1.17 kg·m^{-3}) and dynamic viscosity (μ_G, 1.812×10^{-5} Pa·s) data at 30 °C used for calculations are published by Monnier and Falk (2011).

$$Re_G = \frac{\rho_G \bar{u}_G d_{H,G}}{\mu_G} \tag{S8}$$

$$\bar{u}_G = \frac{Q_G}{\Omega_G} = \frac{Q_G}{w_G \delta_G} \tag{S9}$$

$$d_{H,G} = \frac{4(\delta_G w_G + n_C w_C (d_C - \delta_L))}{2[(w_G + \delta_G) + n_C (w_C + d_C - \delta_L)]} \tag{S10}$$

The dimensionless Kapitza number (Ka, Eq 11) is used to characterize liquid films that are laminar and hydrodynamically smooth. Ka is described by a ratio of surface tension of the liquid (σ_L) to viscosity (μ_L). Froude number (Fr, Figure S5 and Eq S12) classifies the flow regime ($Fr < 1$ tranquil, subcritical flow, $Fr =$ transcritical flow, $Fr > 1$ supercritical, shooting flow). In this study, Fr varied between 0.25 and 2.50 (Figure S5). Liquid flow rates Q_L corresponding to each regime have been defined, Figure S5. The Fr number is unity when Q_L equals 3.51×10^{-8} $m^3 \cdot s^{-1}$. Properties of the gas-liquid interface were evaluated from reported correlations and equations. At fully developed laminar gas flow with $Re_G \leq 2$, it is unlikely that turbulent waves form on the liquid surface as result of Kelvin-Helmholtz instabilities. Tendency of a liquid film surface to change from hydrodynamically smooth to laminar wavy character is described in literature by different empirical correlations. The relation $1.88\ Ka^{0.3} \leq Re_L$ is used to calculate that flow regime change from stratified to laminar wavy flow on the microchannel plate ($w_C = 600$ µm) will occur for $Q_L \geq 1.49 \times 10^{-8}$ $m^3 \cdot s^{-1}$ and $Fr \geq 0.71$. In another correlation (Eq S13), the transition to wavy flow at a critical Re number ($Re_{L\ crit}$) is described to depend on FFMR inclination angle. Critical liquid flow rates $Q_{L,crit}$ marking stratified-to-wavy flow regime change at different inclination angle are calculated accordingly to be in the range 0.97 – 1.11 × 10^{-8} $m^3 \cdot s^{-1}$ (Figure S8). Results of flow regime analysis therefore agree in indicating that the experimental conditions (Q_L, Θ) involved transition from smooth to wavy gas-liquid interfaces (Figure S9) (Drosos et al., 2004; Zapke and Kröger, 2000a; Zapke and Kröger, 2000b)

$$Fr = \frac{\rho_L u_L^2}{g(\rho_L - \rho_G)} \tag{S11}$$

$$Ka = \frac{\sigma_L}{\rho_L (v_L^4 g)^{1/3}} \tag{S12}$$

$$Re_{L\,crit} = \frac{5}{6} cot\Theta \tag{S13}$$

S3. Characterization of Oxygen Diffusion and Oxygen Mass Transfer

The gaseous diffusivity of O_2 ($D_{eff\,G}$) in air at 30 °C was estimated by the Chapman-Enskog equation. The calculation of oxygen diffusion coefficient in aqueous phase ($D_{eff\,L}$) was done with the Stokes-Einstein equation, as shown in Table S4. The validity of diffusion models for the falling film miroreactor (Higby's penetration model or Whitman's two film model) can be assessed by the mass Fourier number (*Fo,* Figure S9 and Eq S14), which is the dimensionless ratio of gas residence time (t_G) and time of gas diffusion (τ_D). The modified mass Fourier number of liquid phase (Fo', Eq S15), is plotted in Figure S10 for all the conditions of reactor operation tested (Table 1) (Kashid et al., 2011; Zanfir et al., 2005).

$$Fo = \frac{t_G}{\tau_D} = \frac{L\,D_{G,O_2}}{\bar{u}_G \delta_G^2} \tag{S14}$$

$$Fo' = \frac{t_G}{\tau_D} = \frac{L\,D_{L,O_2}}{|\bar{u}_G - \bar{u}_L| \delta_L^2} \tag{S15}$$

S4. Estimation of the Theoretical Loading of Z_{basic2}_*Tv*DAAO Per Plate

Assuming a completely flat surface, the geometry of the plate implied a total surface area of 3864.2 mm^2. The surface footprint of the Z_{basic2}_*Tv*DAAO was estimated according a square or circle projection (Figure S11). The dimension of the Z_{basic2}_*Tv*DAAO was assessed by using the crystal structure of *Tv*DAAO and structure modeling of Z_{basic2}; structure modeling of Z_{basic2} was done using the NMR structure of Z domain of staphylococcal protein A (Protein Data Bank entry 2SPZ) as the template. Model of Z_{basic2} was constructed by sequence alignment of Z domain and Z_{basic2} using Modeller 9v8. Visualization was done using pymol 0.99rc6. The plain plate area of the plate (3864.2 mm^2) divided by the enzyme area gave the number of enzyme molecules per plate, which can be transferred with the Avogadro's constant and the turnover number (k_{cat} = 95 s^{-1}; Wiesbauer et al., 2011) into the theoretical activity loading per plate (see Table S3).

Supporting Tables

Table S1. Geometry Parameters of the FFMR

Parameter	Dimension
Depth of liquid channel (d_C)	0.2×10^{-3} m
Channel length (L_C)	76.0×10^{-3} m
Aerated channel length (L)	65.0×10^{-3} m
Number of channels (n_C)	32
Width of gas channel (w_G)	26.0×10^{-3} m
Width of liquid channel (w_L)	0.6×10^{-3} m
Gas channel thickness (δ_G)	5.9×10^{-3} m

Table S2. Physical Parameters of the Gas and Liquid Phases Used

Fluid	Density (ρ), kg·m^{-3}	Kinematic viscosity (ν), m^2·s^{-1}	Contact angle (θ), °	Surface tension (σ), N·m^{-1}
50 mM potassium phosphate buffer, pH 8, 30 ºC	1003.7	7.725×10^{-7}	97.5	0.07149
25 mM D-Ala in 50 mM potassium phosphate buffer, pH 8, 30 ºC	1005.4	7.733×10^{-7}	100.7	0.07056
0.25 mM Pyruvate in 50 mM potassium phosphate buffer, pH 8, 30 ºC	1004.0	9.684×10^{-7}	98.4	0.07131
Immobilization mixture	1047.6	9.319×10^{-7}	90.9	0.02926
Air, 30 ºC	1.17	1.548×10^{-5}	n.a.	n.a.

Table S3. Theoretical and Experimental Loading of Z$_{basic2}$_*Tv*DAAO on the Assumed Smooth Surface of the Microchannel Plate

	*Tv*DAO area, nm^2		Loaded Z$_{basic2}$_*Tv*DAAO activity, U per plate	Loaded Z$_{basic2}$_*Tv*DAAO, mg·m^{-2}
	min	max		
Experimental			0.60 – 1.10	2.67 – 4.89
Footprint (square)	52.2	57.0	0.64 – 0.70	2.85 – 3.12
Footprint (circle)	28.3	30.2	1.43 – 1.52	6.35 – 6.78

Details of the calculation can be found in section S4. Figure S11 illustrates the footprint of Z$_{basic2}$_*Tv*DAAO according to square or circle projection.

Table S4. Diffusion Coefficients of Oxygen

	Gaseous diffusivity of O_2 ($D_{\mathrm{eff\ G}}$), $m^2 \cdot s^{-1}$	Diffusion coefficient of oxygen in aqueous phase ($D_{\mathrm{eff\ L}}$), $m^2 \cdot s^{-1}$
Calculated diffusivity at 30 °C	2.11×10^{-5}	1.28×10^{-9}
Diffusivity at 25 °C given by (Cussler, 2009)	1.76×10^{-5}	2.10×10^{-9}

Table S5. Calculated Mass Transfer Coefficients.

Operation condition	$K_{L,}$ 10^{-5} m·s^{-1} Film theory	$K_{L,}$ 10^{-5} m·s^{-1} Penetration theory	K_La, s^{-1} Film theory	K_La, s^{-1} Penetration theory
Θ, 30°; $Q_{L,}$ 0.82–8.50 x 10^{-8} m^3·s^{-1}	1.2–2.18	2.57–2.73	0.17–0.56	0.32
Θ, 45°; $Q_{L,}$ 1.6–4.0 x 10^{-8} m^3·s^{-1}	1.71–1.96	2.09–2.25	0.34–0.45	0.38
Θ, 90 °; Q_L, 0.82–8.5010^{-8} m^3·s^{-1}	1.34–2.75	2.88–3.07	0.21–0.88	0.45
Θ, 5–90°; Q_L, 0.98 x 10^{-8} m^3·s^{-1}	1.15–1.81	1.25–1.50	0.15–0.38	0.26–0.45

Calculation of K_L values was performed according to equations 2 and 3 at the conditions where penetration model or film model were applicable (section S3). Figure S10 displays the modified mass Fourier number and conditions where theory is applicable.

Supporting Figures

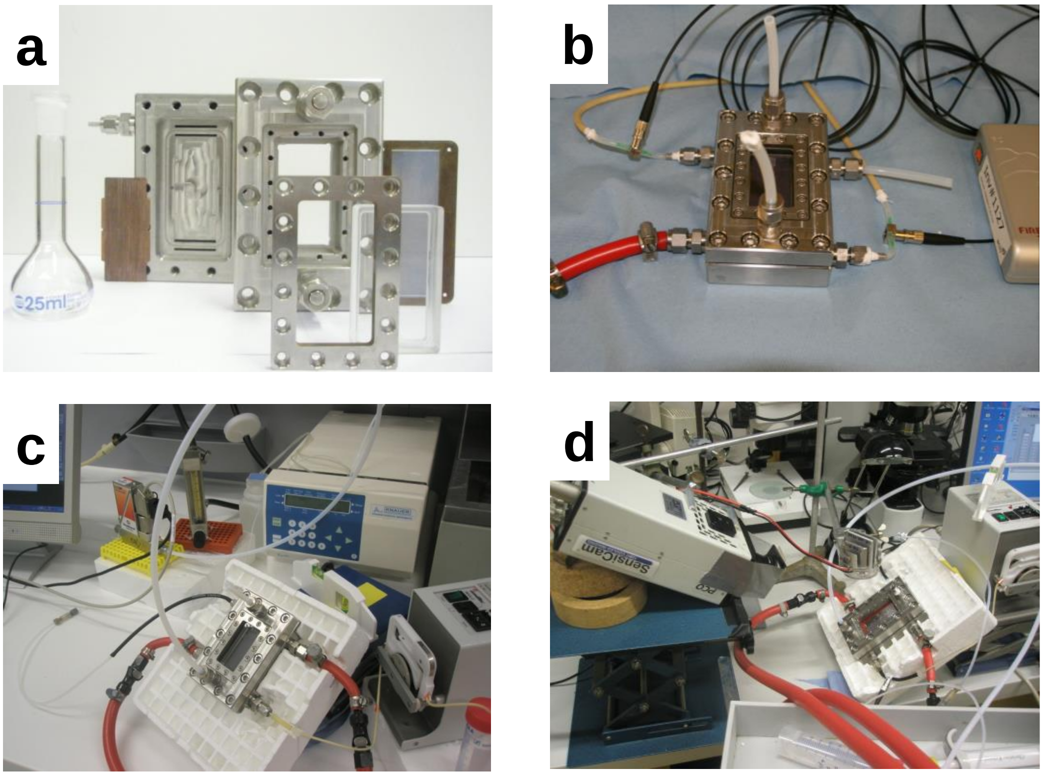

Figure S1. Photographs showing the FFMR set-up are displayed. a) Disassembled FFMR; b) Assembled FFMR instrumented with flow-through oxygen sensors; c) Assembled and instrumented FFMR connected to air and liquid supply; d) Assembled FFMR under operation integrated with luminescence lifetime imaging.

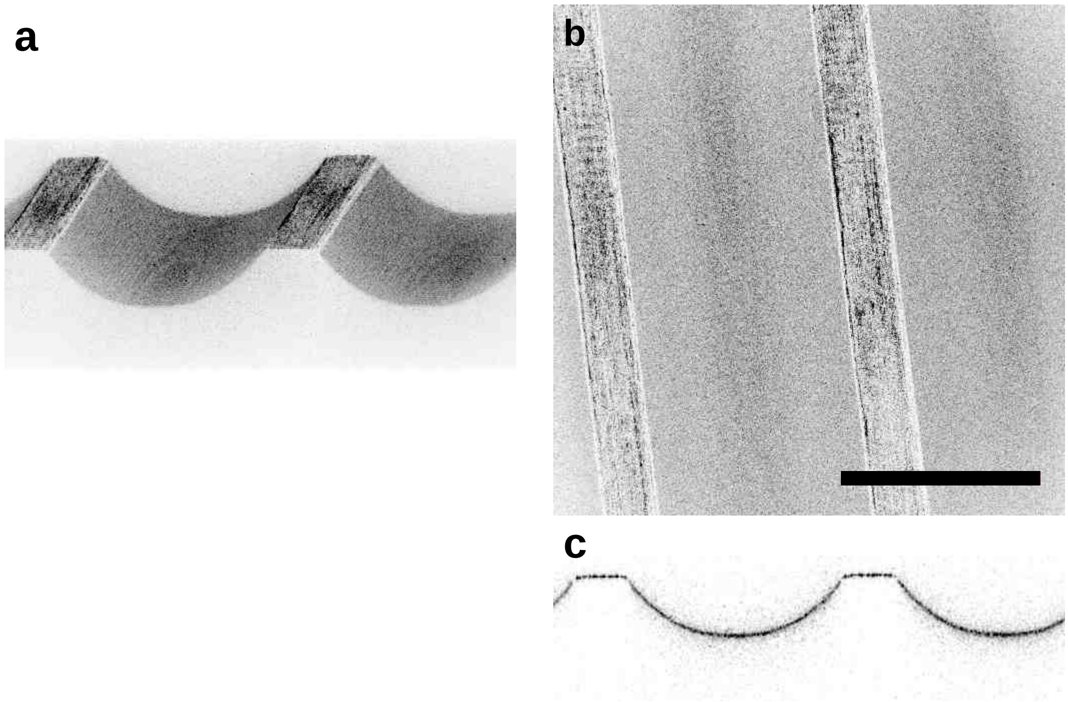

Figure S2. Confocal laser-scanning microscopic images of the dry FFMR plate are shown. The scale bars indicate 600 µm. a) 3D projection of Z-stacked images; b) Z projection of Z-stacked images; c) Orthogonal view of Z-stacked images.

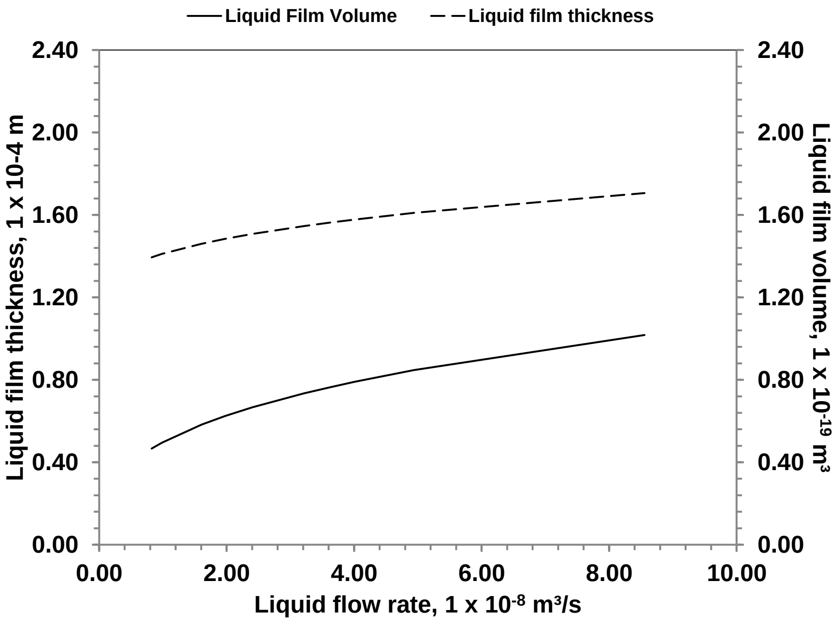

Figure S3. Calculated liquid volume (V_L) and liquid film thickness (δ_L) in dependence on the used flow rate (Q_L) of liquid. The liquid contained 25 mM D-Ala in 50 mM potassium phosphate buffer, pH 8.0. The temperature was 30 °C. The reactor was used an in vertical reactor position. Calculations were performed using equations S1 and S2, as described in section S2.

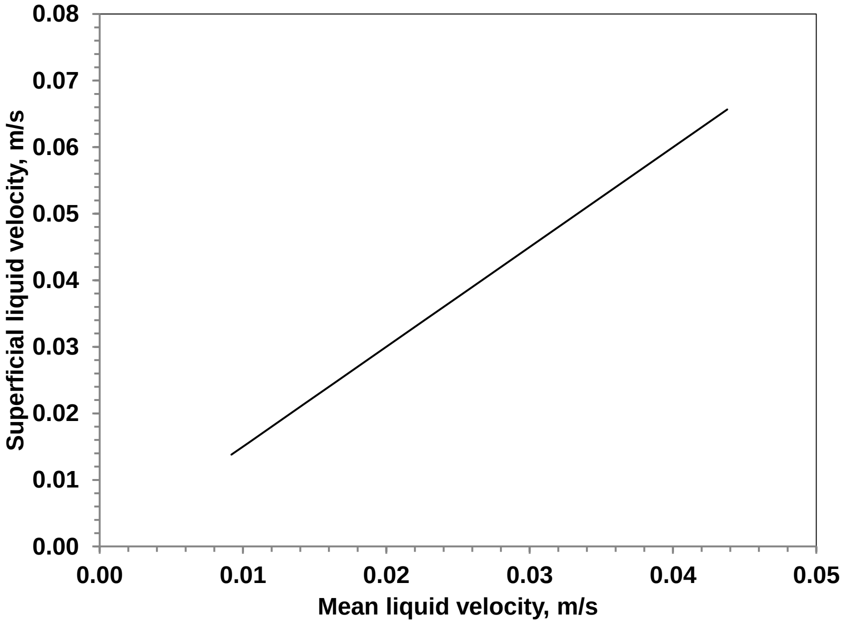

Figure S4. Mean (u_L) and superficial (u) liquid velocities were calculated for the range of liquid flow rates used (Q_L). Calculations were performed using equations S4 and S5 as described in section S2.

(a)

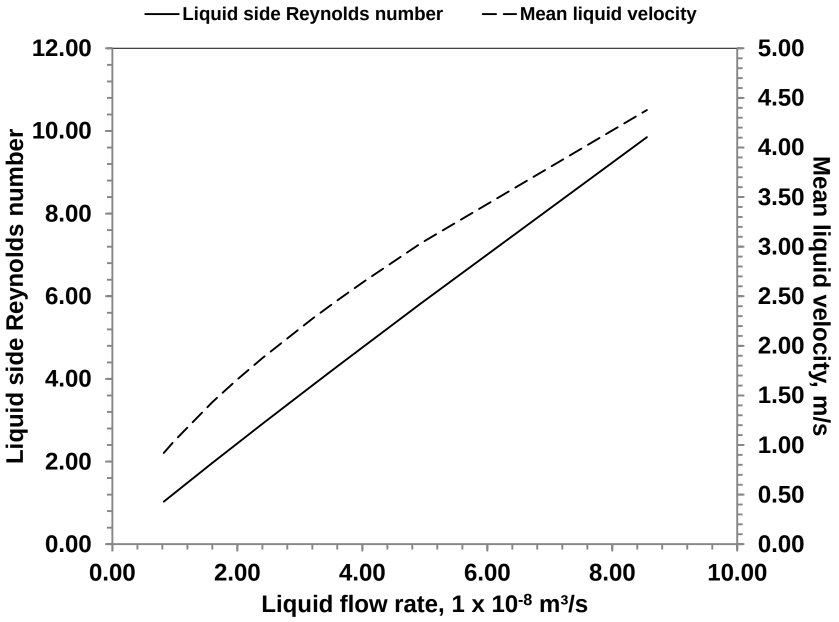

(b)

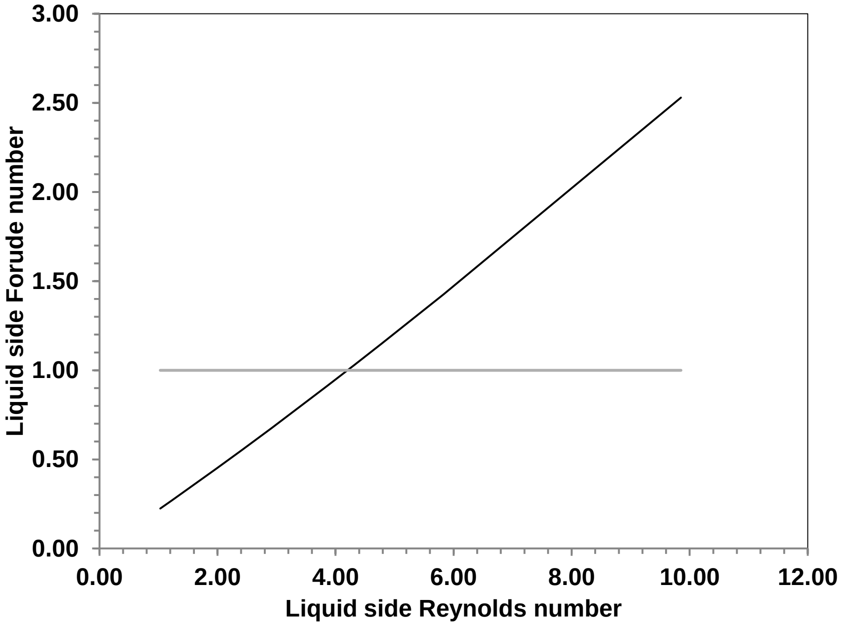

Figure S5. Panel shows the calculated liquid side Reynolds number (Re_L) and the mean liquid velocity (u_L) in dependence on the flow rates of liquid containing 25 mM D-Ala in 50 mM potassium phosphate buffer, pH 8.0. Panel b shows mass Froude number (*Fr*), transcritical mass Froude number $Fr = 1$ is indicated as grey line. Calculations were performed using equations S4, S6 and S11 as described in section S2.

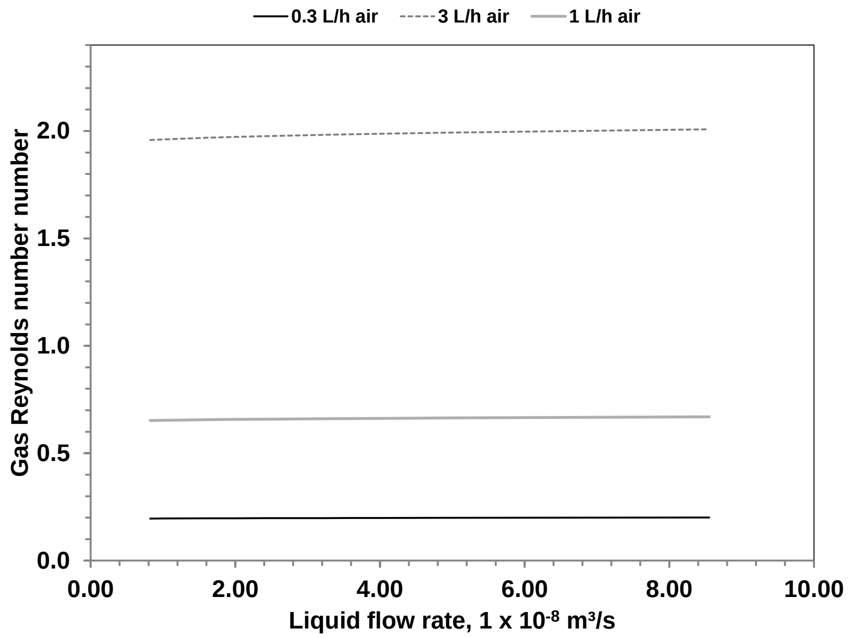

Figure S6. Calculated gas side Reynolds numbers (Re_G) in dependence on the used air flow rates (Q_G). Calculations were performed using equation S8 as described in section S2.

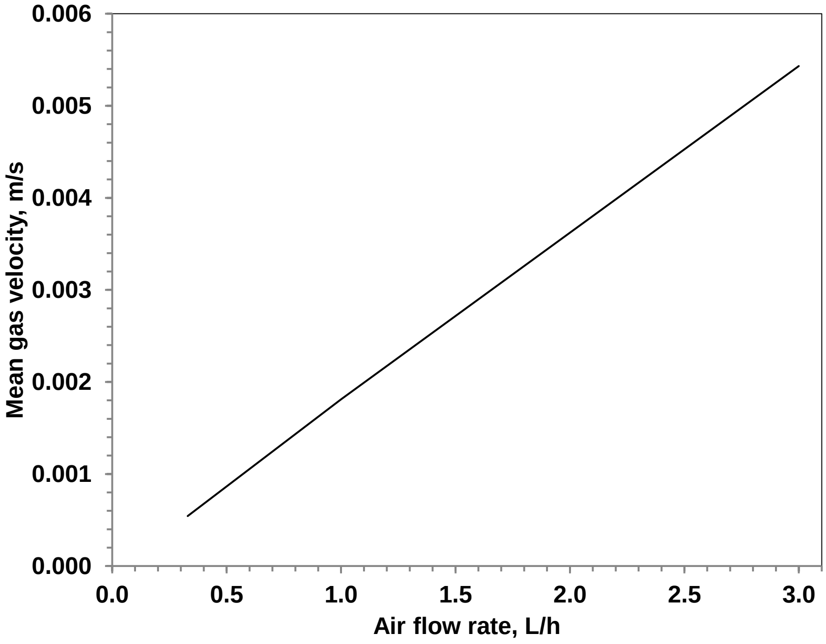

Figure S7. Calculated mean gas velocity (u_G) in dependency on the used air flow rates (Q_G). Calculations were performed using equation S9 as described in section S2.

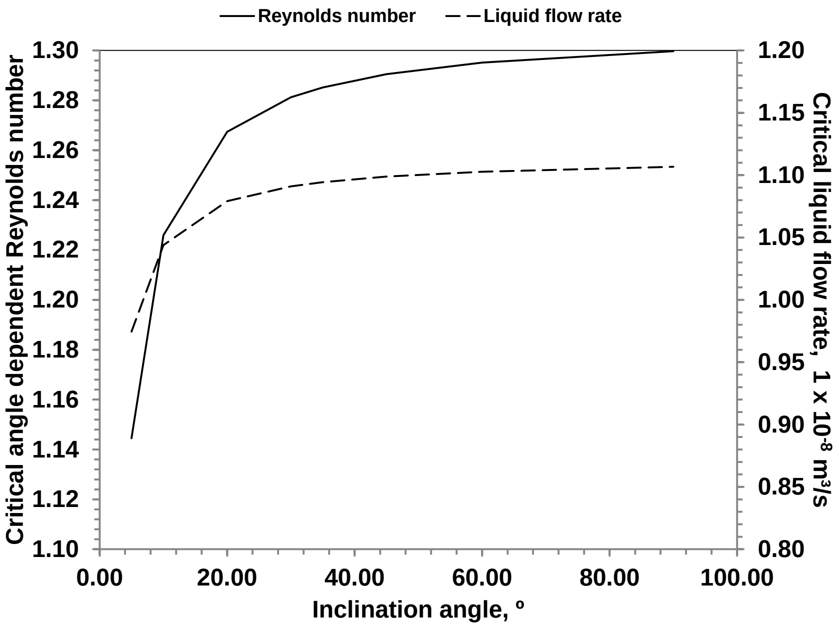

Figure S8. Critical Reynolds number ($Re_{\mathrm{L\ crit}}$) dependent on inclination angle (Θ) are shown. Calculations were performed using equation S13 as described in section S2.

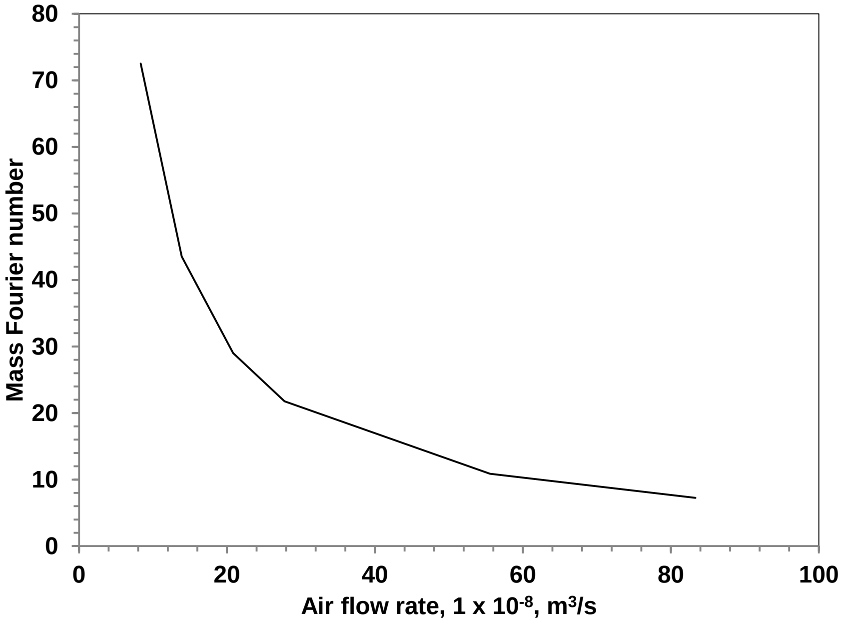

Figure S9. Gas side mass Fourier number (*Fo*). Calculations were performed using equation S14 as described in section S2.

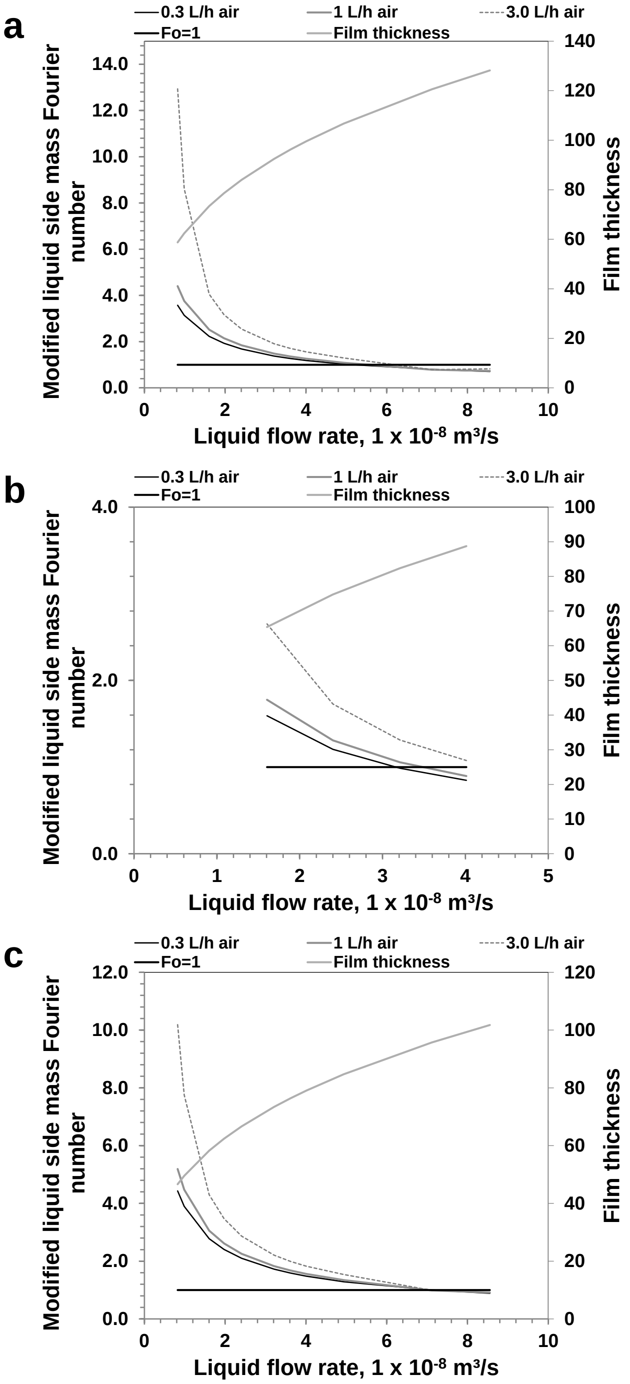

Figure S10. Modified liquid side Fourier number (*Fo´*) for operation of FFMR at varying inclination angle (Θ), 30 º(a), 45 º(b), 90 º(c). The critical *Fo´*=1 is indicated as black. Film thickness (δ_L) is indicated in μm. Calculations were performed using equation S15 and as described in section S2 for all the conditions mentioned in Table1 and Table S5.

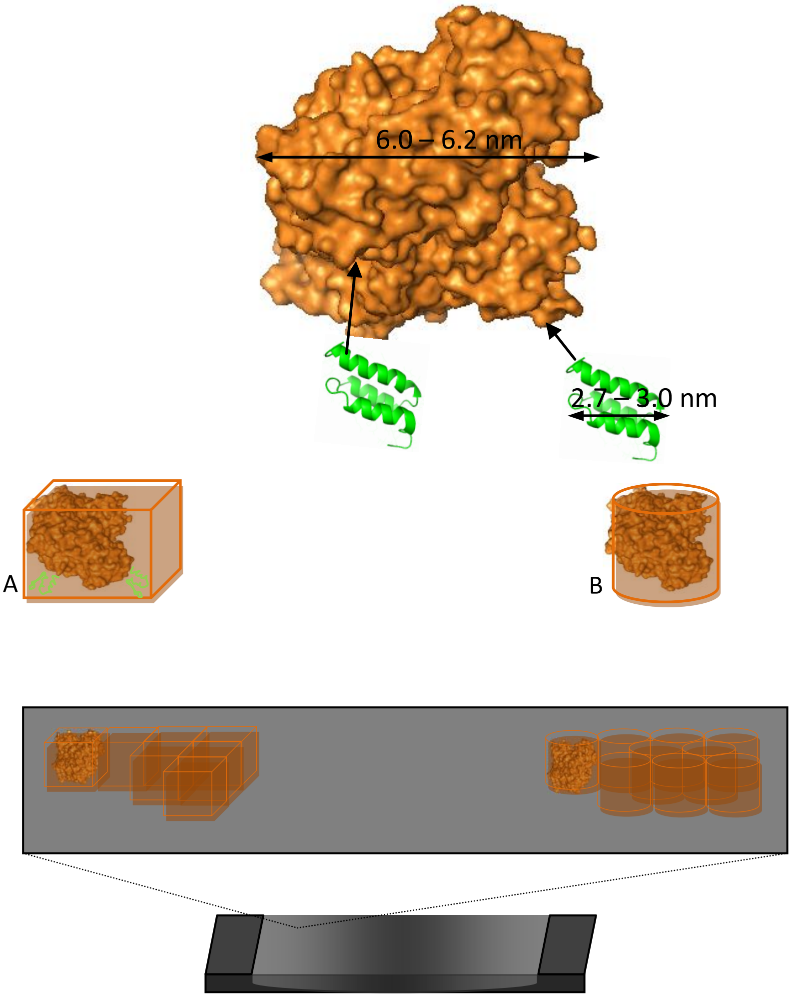

Figure S11. Theoretical maximum loading of Z$_{basic2}$_*Tv*DAAO on the microchannel plate assuming square footprint (a) or circular footprint (b).

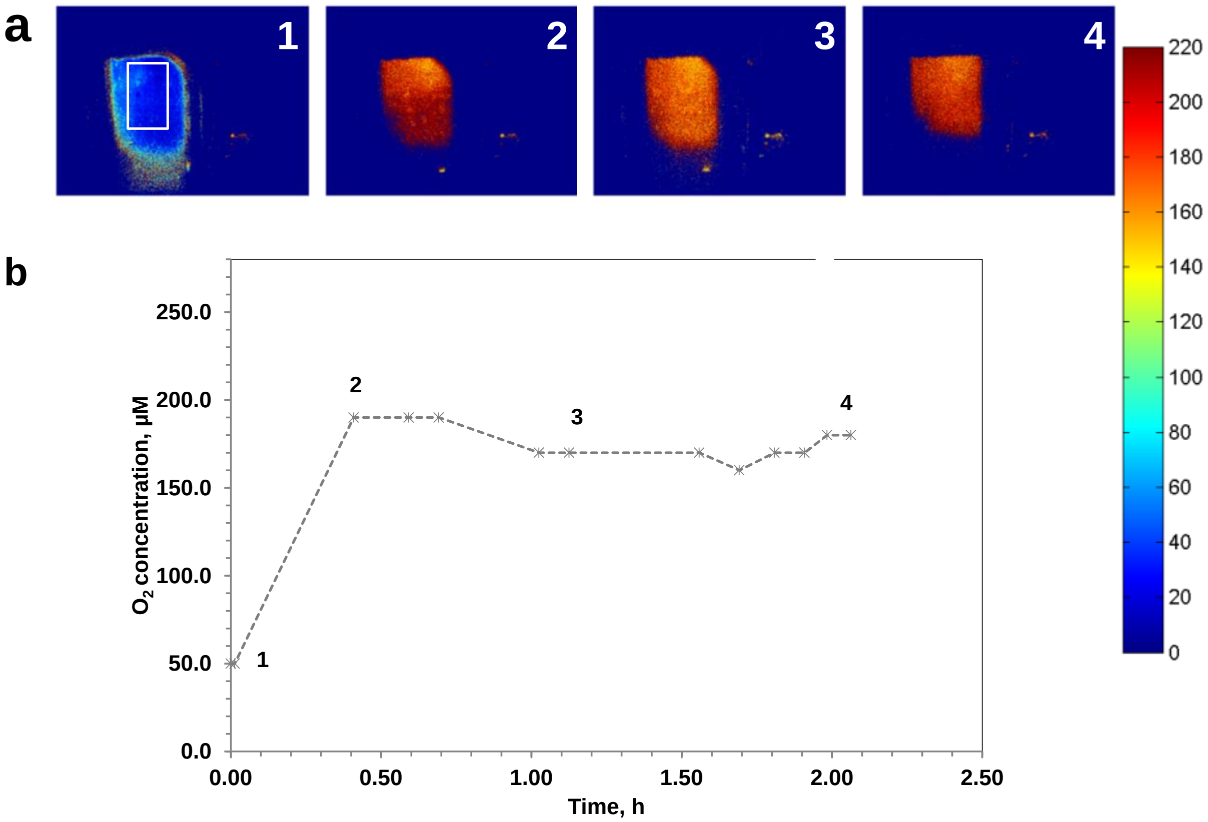

Figure S12. Results of internal and external O_2 concentration measurements during operation of the FFMR containing immobilized Z_{basic2}_*Tv*DAAO (1.1 unit) are shown. The reactor was operated at 1.97 × 10^{-8} $m^{3}\cdot s^{-1}$ of liquid flow (25 mM D-Ala) and 45 ° of reactor inclination angle Θ. Panel a shows the local O_2 concentration on the plate in hPa (1 hPa is equivalent to 1.16 µM at 30ºC). The region of interest for measurement comprises a rectangle of 14.8 mm × 23.5 mm located at the lower end of the plate, as indicated in the image #1 of panel a. Panel b shows on-plate O_2 concentration measurements. Numbering is used to identify images from the upper panel that correspond to the local O_2 concentrations shown in the lower panel. During the first area show in panel b the FFMR was operated with nitrogen flow showing total deoxygenation in the plate. Opening up the gas ports to enable air to enter in the absence of controlled gas flow, the internal O_2 concentration increased constantly again (measurements #1 - #4). An extremely high oxygenation capacity of the FFMR is demonstrated.

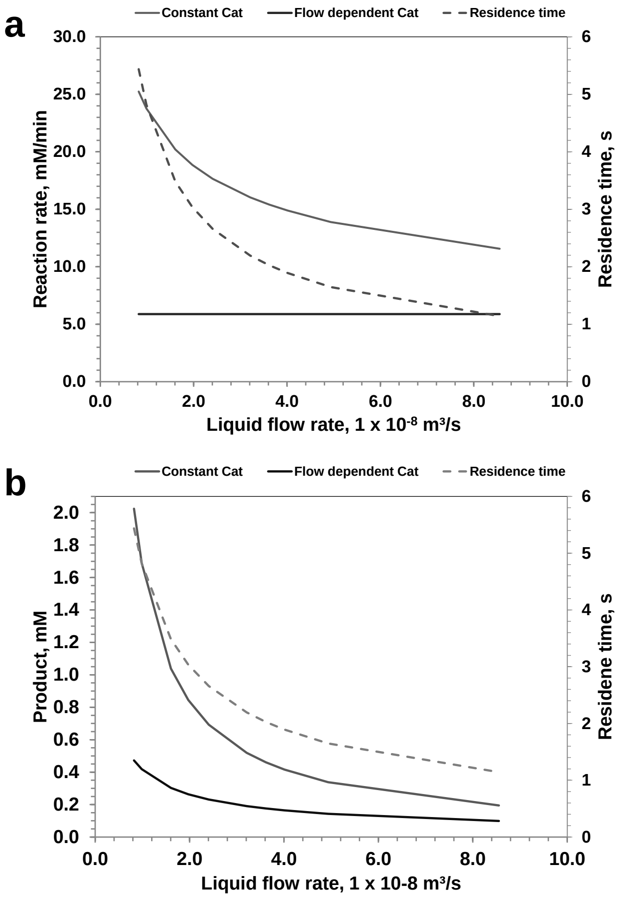

Figure S13. Calculated reaction rates (a) and product concentrations (b) formed during the oxidation of D-Ala catalyzed by Zbasic2_DAAO immobilized in the FFMR. Calculations are performed for 1.1 catalytic units. Assuming ideal plug flow of the liquid phase, performance of the reactor at steady state was modeled, expressing the product concentration *P* with the relationship, $P = (AL_c/Q_L)(Cat/V_L)$, where *A* is the cross-sectional area of the liquid phase (m^2) and *Cat* is the enzyme activity used in the reaction (1.83×10^{-8} mol·s^{-1}),. Like V_L, *A* is dependent on Q_L. The degree of wetting of the microchannel walls depends on V_L, hence *A*. In the case that immobilized enzyme is distributed homogeneously on the wall surface, the degree of channel wetting determines to which extent the immobilized enzyme is utilized under given reaction conditions, that is, the effectively used $Cat\ (Q_L) \leq Cat$. A directly proportional dependence of *Cat* on V_L was used. The alternative scenario considered was that *Cat* was not dependent on Q_L and Θ, as would be the case if all of the enzymes were immobilized at the bottom surface of the microchannel. The calculations were performed for inclination angle of 90º. Total oxygen saturation of liquid phase is assumed. Liquid phase contains 25 mM D-Ala in 50 mM potassium phosphate, pH 8.0, at 30 ºC.

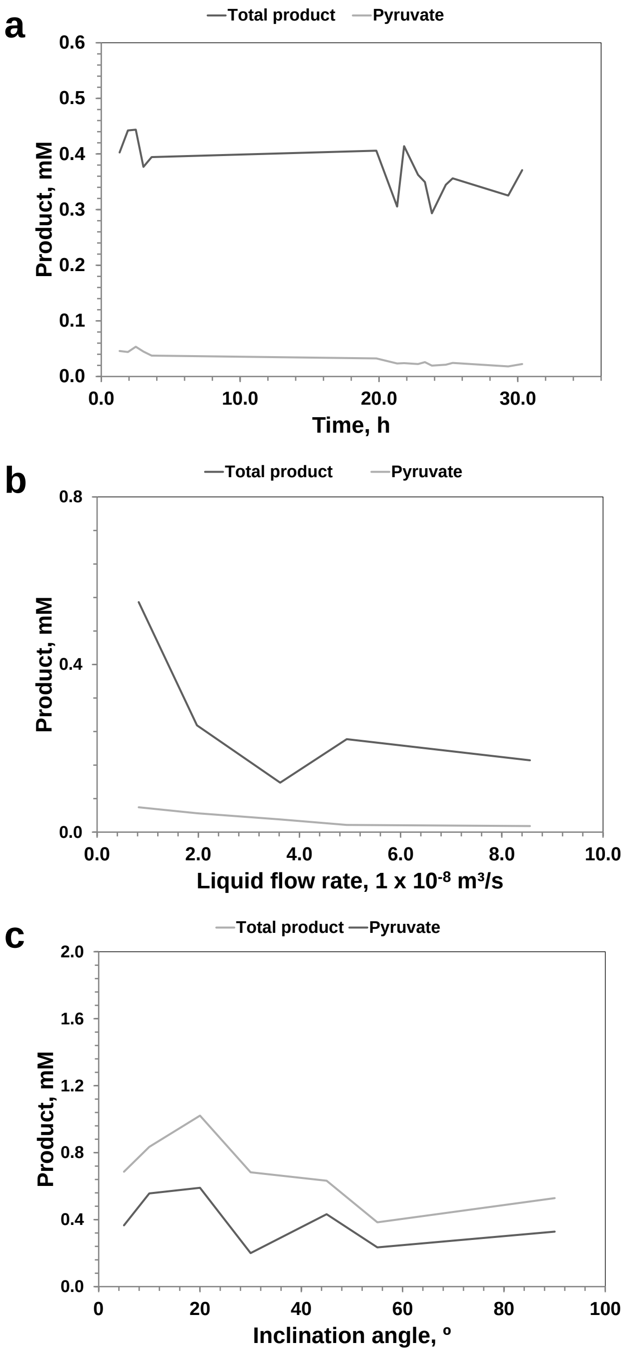

Figure S14. The product concentration released on oxidation of D-Ala in the FFMR containing immobilized Z_{basic2}_*Tv*DAAO (1.1 units) is shown. The substrate concentration was 25 mM D-Ala. A time course of conversion is shown in panel a ($Q_L = 3.21 \times 10^{-8}$ m^3·s^{-1}, $\Theta = 45^o$, Q_G = 1.0 L/h). The reactor was also operated at variable liquid flow (panel b, $\Theta = 30^o$) and inclination angle (panel c, Q_L=0.98 × 10^{-8} m^3·s^{-1}) and product concentrations at apparent steady state are shown. Addition of catalase was implemented in panel b and c to minimize product decarboxylation.

List of symbols

a: interfacial area, m^{-1}

d_C: depth of liquid channel, m

$d_{H,G:}$ hydraulic diameter of gas, m

$d_{H,L}$: hydraulic diameter of liquid, m

$D_{G,O2:}$ gaseous diffusivity of O_2, $m^2 \cdot s^{-1}$

$D_{L,O2}$: diffusion coefficient of O_2 in the liquid phase, $m^2 \cdot s^{-1}$

g: gravitational acceleration, $m \cdot s^{-1}$

Fo: mass Fourier number

$Fo´$: liquid side modified mass Fourier number

Fr: Froude number

Ka: Kapitza number

K_L: liquid side mass transfer coefficient, $m \cdot s^{-1}$

$K_L a$: volumetric mass transfer coefficient, s^{-1}

L: aerated channel length, m

L_c: channel length, m

n_c: number of channels

Q_G: gas flow rate, $L \cdot h^{-1}$

Q_L: liquid flow rate, $m^3 \cdot s^{-1}$

Re_G: gas-side Reynolds number

Re_L: liquid-side Reynolds number

$Re_{L\ crit}$: critical liquid-side Reynolds number

$t_{G:}$ gas residence time, s^{-1}

u_G, mean velocity of the streaming air, $m \cdot s^{-1}$

u: superficial fluid velocity, $m \cdot s^{-1}$

$u_{L:}$ mean liquid velocity rate, $m \cdot s^{-1}$

$\nu_{L,}$ kinematic viscosity of liquid phase, $m^2 \cdot s^{-1}$

V_L: liquid volume, mL

w_C: microchannel width, m

w_G: gas chamber width, m

δ_G: gas channel thickness, m

δ_L: liquid film thickness, m

θ: contact angle, º

Θ: reactor inclination angle, º

μ_L: dynamic viscosity of liquid

μ_G: dynamic viscosity of gas, Pa·s

$\rho_{G:}$ air density, kg·m^{-3}

ρ_L: density of liquid phase, kg·m^{-3}

σ_L: tension of the liquid, N·m^{-1}

τ_D: time of gas diffusion, s^{-1}

Ω_G: cross-sectional area of the gas phase, m

Supporting references

Commenge J-M, Obein T, Framboisier X, Rode S, Pitiot P, Matlosz M. 2011. Gas-phase mass-transfer measurements in a falling-film microreactor. Chem Eng Sci 66:1212–1218.

Commenge J-M, Obein T, Genin G, Framboisier X, Rode S, Schanen V, Pitiot P, Matlosz M. 2006. Gas-phase residence time distribution in a falling-film microreactor. Chem Eng Sci 61:597–604.

Cussler EL. 2009. Diffusion: mass transfer in fluid systems 3rd ed. Cambridge ; New York: Cambridge University Press 631 p.

Drosos EI., Paras S., Karabelas A. 2004. Characteristics of developing free falling films at intermediate Reynolds and high Kapitza numbers. Int J Multiph Flow 30:853–876.

Kashid MN, Renken A, Kiwi-Minsker L. 2011. Gas–liquid and liquid–liquid mass transfer in microstructured reactors. Chem Eng Sci 66:3876–3897.

Mhiri N, Monnier H, Falk L. 2011. Intensification of the G/L absorption in microstructured falling film application to the treatment of chlorinated VOC’s. art III: Influence of gas thickness channel on mass transfer. Chem Eng Sci 66:5989–6001.

Monnier H, Falk L, Lapicque F, Hadjoudj R, Roizard C. 2010. Intensification of G/L absorption in microstructured falling film. Application to the treatment of chlorinated VOC’s – part I: Comparison between structured and microstructured packings in absorption devices. Chem Eng Sci 65:6425–6434.

Monnier H, Falk L. 2011. Intensification of G/L absorption in microstructured falling film. Application to the treatment of chlorinated VOC’s - part II: Modeling and geometric optimization. Chem Eng Sci 66:2475–2490.

Nourmohammadi A, Asadabadi SJ, Yousefi MH, Ghasemzadeh M. 2012. Photoluminescence emission of nanoporous anodic aluminum oxide films prepared in phosphoric acid. Nanoscale Res Lett 7:689.

Schagen A, Modigell M. 2004. Luminescence technique for the measurement of local concentration distribution in thin liquid films. Exp Fluids 38:174–184.

Wiesbauer J, Bolivar JM, Mueller M, Schiller M, Nidetzky B. 2011. Oriented immobilization of enzymes made fit for applied biocatalysis: Non-covalent attachment to anionic supports using Zbasic2 module. ChemCatChem 3:1299–1303.

Yeong KK, Gavriilidis A, Zapf R, Kost H-J, Hessel V, Boyde A. 2006. Characterisation of liquid film in a microstructured falling film reactor using laser scanning confocal microscopy. Exp Therm Fluid Sci 30:463–472.

Zanfir M, Gavriilidis A, Wille C, Hessel V. 2005. Carbon dioxide absorption in a falling film microstructured reactor: Experiments and modeling. Ind Eng Chem Res 44:1742–1751.

Zapke A, Kröger D. 2000a. Countercurrent gas–liquid flow in inclined and vertical ducts — II: The validity of the Froude–Ohnesorge number correlation for flooding. Int J Multiph Flow 26:1457–1468.

Zapke A, Kröger DG. 2000b. Countercurrent gas–liquid flow in inclined and vertical ducts — I: Flow patterns, pressure drop characteristics and flooding. Int J Multiph Flow 26:1439–1455.